PIV Measurements of Shock-Wave/Boundary-Layer Interactions at Mach 2.5 in a Circular Test Section

Heath H. Reising* and David O. Davis*
NASA Glenn Research Center, Cleveland, OH, 44135

The particle image velocimetry (PIV) measurement technique has been applied to make detailed measurements in an impinging shock-wave/boundary-layer interaction (SWBLI) flowfield in a test section of circular cross-section. By virtue of this test section geometry, the flowfields studied are free from effects of the complex coupling of sidewall and corner interaction into the primary impinging shock interaction typical of a rectangular test section. The cone-cylinder shock generator hardware was arranged in both coaxial alignment with the test section to generate axisymmetric SWBLIs and in offset positions to generate swept SWBLIs. The angle of the conical section was also varied to alter the strength of the impinging shock wave. The application of the PIV technique in this test section required meticulous design to provide adequate optical access without disturbing the SWBLI flow. Details of the stereoscopic PIV apparatus and the velocity measurements obtained for a Mach 2.5 freestream are presented. Key features of the mean velocity and turbulent stress fields are highlighted. This data set should enable validation of computational fluid dynamics results for these flowfields.

Nomenclature

c_D = particle drag coefficient, $\frac{\vec{F}_{D,p}}{-\frac{\pi}{8} d_p^2 \rho_f \left\|\vec{U}_p - \vec{U}_f\right\| \left(\vec{U}_p - \vec{U}_f\right)}$
c_f = boundary layer friction coefficient, $\frac{\tau_w}{\frac{1}{2}\rho_\infty U_\infty^2}$
$\vec{d}$ = PIV stereoscopic reconstruction error
$\vec{F}_{D,p}$ = particle drag force
f_{Kn} = Cunningham correction factor for particle drag in the non-continuum regime
Kn = Knudsen number
ℓ = shock generator offset distance from test section axis
P = pressure
R = test section radius, 8.5 cm
Re_D = core flow Reynolds number based on test section hydraulic diameter ($2R$)
Re_p = particle slip Reynolds number, $\frac{\left\|\vec{U}_p - \vec{U}_f\right\| d_p}{\nu_f}$
Re_{δ_2} = boundary layer characteristic Reynolds number using wall viscosity, $\frac{U_\infty \theta}{\nu_w}$
Re_θ = boundary layer momentum thickness Reynolds number, $\frac{U_\infty \theta}{\nu_\infty}$
Re_τ = boundary layer outer Reynolds number, $\frac{u_\tau \delta_{99}}{\nu_w}$
T = temperature
U = axial velocity (aligned with $\vec{x}$)
u_τ = boundary layer friction velocity, $\sqrt{\frac{\tau_w}{\rho_w}}$
V = vertical velocity (aligned with $\vec{y}$)
W = spanwise velocity (aligned with $\vec{z}$)
x = axial coordinate, $x = 0$ at leading edge of test section
y = vertical coordinate, $y = 0$ on test section axis
$\overline{y}$ = wall-normal coordinate, $\overline{y} = 0$ at $(r, \theta) = (R, 180^\circ)$
z = spanwise coordinate, $z = 0$ on test section axis

*Aerospace Engineer, Inlets and Nozzles Branch, 21000 Brookpark Rd M/S 5-12, AIAA Senior Member.

α = shock generator cone half-angle
δ = boundary layer thickness based on $\overline{y}(U = 0.99U_\infty)$
δ^* = boundary layer displacement thickness
θ = boundary layer momentum thickness or azimuth in cylindrical coordinate system, $\theta = 0$ at 12 o'clock and is clockwise positive looking upstream
$\overline{\theta}$ = shock generator azimuth relative to PIV measurement region
Π = turbulent boundary layer wake parameter
ρ = density
τ_w = wall shear stress, $\mu_w \left(\frac{\partial U}{\partial y}\right)_w$

Superscripts

$+$ = inner-scaling units

Subscripts

0 = facility nozzle exit station
1 = station at which incoming boundary layer is evaluated
∞ = freestream or boundary layer edge
f = fluid
i = inviscid shock impingement
p = particle
r = recovery
rms = root-mean-square
t = total condition
w = wall

I. Introduction

Validation of turbulence models is paramount in the pursuit of accurate computational fluid dynamics (CFD) predictions in the complex flowfields present in realistic aerospace vehicle and propulsion designs. Typically, methods which rely on modeling of the more complex fluid physics (e.g. Reynolds stresses and heat flux vector in Reynolds-averaged Navier-Stokes (RANS) simulations) are less computationally expensive and can be used in parametric optimization studies. However, the models used within these lower-fidelity methods are almost universally calibrated in equilibrium turbulence and require careful tuning to accurately predict the production, transport, and dissipation of turbulence in complex flowfields. Shock-wave/boundary-layer interactions are typically identified as a problematic case for RANS solvers due to their large departure from an equilibrium turbulence state [1].

A dearth of high quality experimental data in supersonic and hypersonic shock-wave/boundary-layer interactions for use in code validation efforts was identified by Settles and Dodson [2]. There, many of the candidate datasets were rejected due to the lack of well-defined boundary conditions, undocumented 3D effects, inconsistency between repeated measurements, or a lack of repeated measurements. A specific methodology was laid out in Ref. 3 for planning useful CFD code validation experiments which acknowledges the interdependency between the requirements and capabilities of experimental and computational results.

In addition to the overall lack of high-quality experimental data, there are also issues with sidewall influences in many nominally 2D SWBLI datasets. References 4 and 5 show just two examples where blockage generated by corner separations influence the strength of the primary SWBLI. Thus, the current campaign aims to use an axisymmetric wind tunnel test section and shock generator cone to circumvent this issue.

The Turbulent Computational Fluid Dynamics Validation Experiment (TCFDVE) has been an ongoing effort funded by the Transformational Tools and Technologies Project at the NASA Glenn Research Center (GRC) to provide a high-quality experimental dataset of a SWBLI which is free of sidewall effects. Previous work on the TCFDVE in the NASA GRC 225 cm^2 Wind Tunnel utilized oil flow visualization, wall static pressure distributions, Pitot probe surveys, and hot-wire probe surveys to provide a detailed characterization of several SWBLIs in an axisymmetric test section [6, 7] at Mach 2.5. An important component of a high-quality CFD validation dataset is the corroboration of a multitude of independent redundant measurements. Thus, in addition to the Pitot and hot-wire datasets, particle image velocimetry (PIV) was selected as a measurement technique for the validation dataset because:

1) it provides a direct measurement of flow velocity,
2) it is non-intrusive measurement and, thus, eliminates probe effects,
3) is capable of collecting large 2D fields of dense data in a short period, and
4) can simultaneously measure all 3 velocity components.

This report summarizes the velocity measurements obtained using the PIV technique in both axisymmetric and swept SWBLIs at a freestream Mach number of 2.5.

II. Apparatus and Procedure

A schematic of the flowfield being studied is shown in Fig. 1. Simple cone-cylinder bodies were used to generate the initial shock wave which impinges on the naturally-occurring test section boundary layer. This provides a relatively thick profile in which to perform the detailed measurements required. The cone half-angle, α, was varied to provide both unseparated and separated interactions. A variable offset of the body, ℓ, was provided through the mounting strut which allowed for the generation of both axisymmetric and swept interactions. The strut supporting the cone-cylinder was also rotatable about the test section z-axis.

The details of the shock generator geometry and mounting are presented in Section II.B. The axisymmetric case requires sampling only in one x-r plane to fully describe the flowfield (symmetry of the freestream flow was verified in Ref. 6). Also, by rotating the support strut in θ, the entire swept shock flowfield may be rotated by moving the shock generator body to various azimuthal positions. This allows for complete surveying of the flowfield with measurements capable only of surveying in one x-r plane. For the TCFDVE campaign, the near-wall measurements were made at the $\theta = 180^\circ$ position. Thus, a secondary vertical coordinate, $\overline{y} = y + R$, is introduced which aligns the presented data with typical wall-referenced coordinates used when presenting boundary layer data. This not only reduced the maximum amount of cantilever required in the traverse system used for probe measurements, but also was key in enabling wider application of PIV in this flowfield.

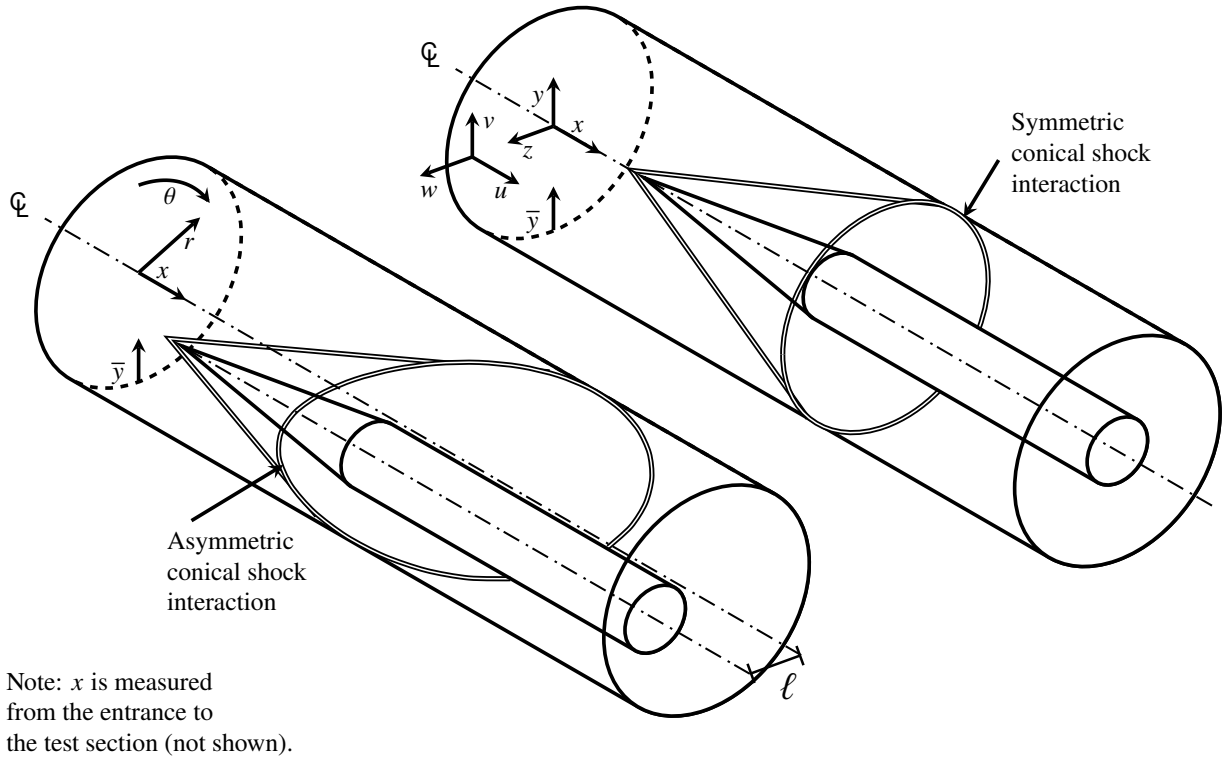


Fig. 1 Basic geometry and coordinate system.

A. Test Facility

The NASA Glenn 225 cm^2 Wind Tunnel is a continuous-flow facility. It utilizes a lab-wide shared pressurized air source which provides clean (filtered to 0.5 µm) and dry (typical dew point of 235–255 K) air at a gauge pressure up to 276 kPa (40 psig). Inlet air may be heated up to 339 K (150 °F) to provide precise control of the total temperature. The facility exhausts to a centralized vacuum source which provides 660 Torr (26 inHg) of vacuum. Test sections with circular, square, and octagonal cross-sections are available with essentially identical cross-sectional area.

For the test results presented herein, the tunnel was configured with its axisymmetric 17 cm diameter test section and a Mach 2.5 converging-diverging nozzle. This is depicted in Fig. 2 below. A new test axisymmetric test section was fabricated for this work which provides the same basic flowpath dimensions as in Refs. 6 and 7, with the addition of window ports for optical access. In order to gain clearance for camera mounting at the extreme angles required, a 203.2 mm long cylindrical spacer was fabricated and installed between the nozzle and test section to allow for the windows to be installed at a more upstream station within the test section. An equal length spacer was added to the cone-cylinder assembly so that the interactions occur at the same axial position as in previous probe testing.

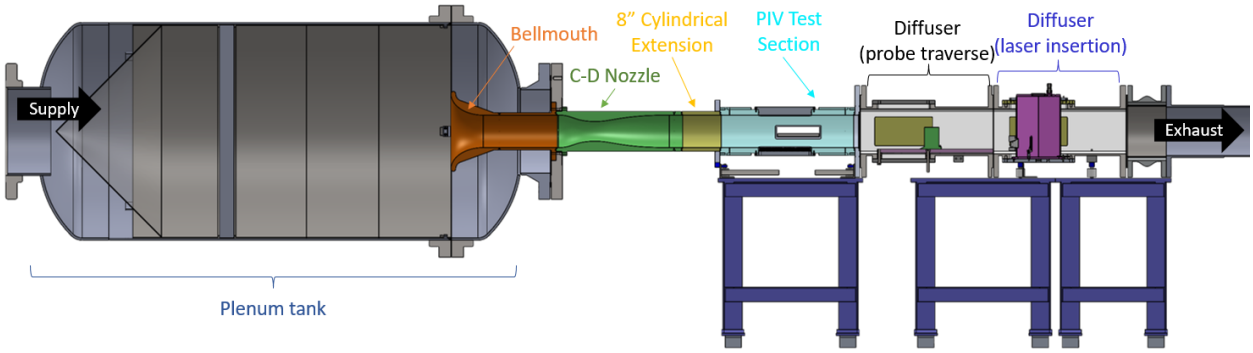
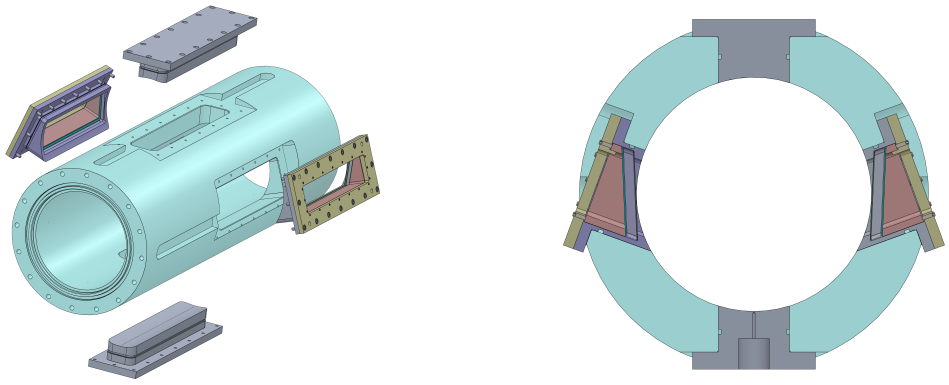


Fig. 2 NASA GRC 225 cm^2 Wind Tunnel as configured for this test.

The PIV test section itself has the same overall length and diameter as the baseline configuration [6, 8]. As shown, a simple cylindrical extension piece was designed to be installed upstream of the PIV version in order to shift an equivalent x station forward within the test section by 8 in (203.2 mm) relative to the baseline. Cutouts for the standard 51.3 mm × 279.4 mm window inserts were placed at $\theta = 0°$ and $\theta = 180°$ as in the baseline test section, but both the port and starboard cutouts were omitted to allow for larger optical windows to be installed. The PIV test section assembly is shown in Fig. 3.

The forward edge of the PIV window cutouts are located at $x = 495.3$ mm($x = 0$ is defined in the TCFDVE campaign to be at the nozzle exit station). By placing the windows aft of the axisymmetric inviscid shock impingement station, the influence of geometry change at the window on the SWBLI region is minimized. The 241.3 mm × 67.4 mm through cuts were made at a 20° downward angle to accommodate the intended PIV measurement being along the test section wall at $\theta = 180°$. Each window assembly consists of an aluminum frame, a 7.6 mm thick piece of fused silica sandwiched between two rubber gaskets, a steel wedged peripheral shim ring, and the aluminum retaining flange. Each window frame was designed to precisely match the inner mold line curvature of the test section, while the nearly tangent glass had inevitable recesses at the top and bottom (maximum depth of 5 mm).

The use of curved windows in this application was eliminated due to the requirement that all test hardware withstand the maximum pressure available in the facility (40 psig). This drove the glass material thickness high enough that a strong lensing effect would be created and image distortion would be insurmountable when combined with the already difficult viewing angles. A "dual-pane" assembly which uses a thin curved flow surface window with an outer pressure-containing flat window could be pursued in future efforts, but was deemed too complex for this entry. The window assemblies were pneumatically pressure tested to avoid moisture-induced crack growth acceleration.



(a) Exploded view. **(b) y-z section view.**

Fig. 3 Axisymmetric test section with optical access for PIV.

B. Shock Generator Hardware

The cone-cylinder centerbodies used to generate the impinging shock waves were highly configurable. Three tip cone half-angles were available to generate interactions of various strengths: 10° for an unseparated interaction, 13.5° for incipient separation, and 16° for a fully separated interaction. The cylindrical portion of the body was 5 cm in diameter and was comprised of a collection of spacer pieces to generate the desired axial length. A specific length of spacer stack was selected for each cone angle to place the inviscid impingement at the same axial station as in Ref. 7. The cone-cylinders were cantilevered from a support strut spanning the aft end of the section. This strut had a sharp leading edge to reduce blockage and, thus, lower the minimum Reynolds number condition available for testing. Three mounting positions are available on the strut. A centerline position allows for the generation of an axisymmetric interaction while two offset positions generate swept interactions as shown in Fig. 1. Figure 4 gives a cross-sectional view of the test section to illustrate the relevant dimensions and variables for positioning the shock generator.

To allow the PIV laser sheet to pass through the support strut when the shock generator is located at $\theta = 0°$ or $\theta = 180°$ position, small (38 mm × 3.8 mm) slits were cut with by wire electrical discharge machining (EDM) though the symmetry plane of the strut. Also, when presenting the PIV measurement results, it is convenient to use an alternative azimuthal coordinate which describes the shock generator position relative to the measurement plane. This is shown as $\overline{\theta}$ in Fig. 4.

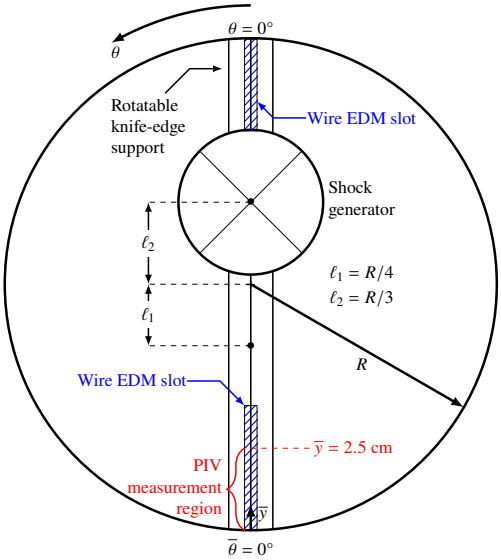


Fig. 4 View looking downstream of test section with shock generator located at $\theta = 0°$ and $\ell = \ell_2$.

C. Conventional Instrumentation

The PIV test section was instrumented with a reduced number of static taps from the conventional version. Ports were drilled 50.8 mm from the forward and aft ends (x = 254 mm and x = 863.6 mm, respectively) at $\theta = 0°$, 90°, 180°, and 270°. However, a highly-instrumented window insert was available for installation in the cutouts at $\theta = 0°$ and 180°. This insert, installed in the $\theta = 0°$ port (opposite the PIV measurement region) during this PIV entry, provided static pressure measurements over x = 412.75–679.45 mm at 3.18 mm spacing.

The static pressure measurements were used in this entry as an in situ confirmation of nominal facility operation since they should provide redundant copies of the data taken in the baseline test section. The reader is referred to Ref. 8 for presentation of the typical static pressure profiles and a thorough analysis.

D. Particle Image Velocimetry Measurement System

The introduction of the planar PIV technique into this test facility was described in detail in Ref. 9. The method by which seed particles would be introduced into the wind tunnel was carefully considered to optimize the PIV measurement quality while minimizing the detriment to existing probe measurement capabilities. The resulting median particle relaxation time was shown to be <3 µs over the range of Reynolds numbers of interest to this study [9]. In addition, to accommodate the selected laser sheet orientation, new hardware was fabricated for installation within the wind tunnel diffuser to allow for laser ingress and to protect the optics which reside within the flowpath. Additional components were added to this system to facilitate longer duration of seeder operation at high Reynolds numbers. The following sections describes the PIV system in detail.

1. Flow Seeding

Seed particles are generated using a condensation-based mineral oil droplet generator (ViCount 2200). This type of seeding device avoids agglomeration of particles in the supply piping, as the oil droplets are generated as the hot oil vapor exits the supply piping. Mineral oil seed material is also a desirable choice for this facility as residual seed material can be removed simply by operating at an elevated temperature and allowing adequate time for oil residue to evaporate from the internal surfaces. In the present study, limiting the seeded region to the lower-center portion of the tunnel keeps the observation windows clean and increases the particle image density in the region of interest. The rake assembly is also mounted to a motorized translation stage for precise positioning during tunnel operation.

2. Laser Sheet

The laser sheet for this study was introduced through a pressurized fairing within a diffuser section downstream of the test section. This allows the laser beam to be sent counter to the wind tunnel flow in the x-y plane while glancing on the bottom of the test section to allow for near-wall measurements of the test section boundary layer with minimal flare. The laser beam was generated by a dual head frequency-doubled Nd:YAG laser (Quantel Evergreen 200). The beam is expanded vertically by a pair of cylindrical lenses and focused to a thin sheet by a 2 m focal length spherical lens. This results in a collimated laser sheet which is 32 mm high at the measurement region.

In order to protect the final laser mirror which is mounted within the tunnel flowpath, a protective fairing was fabricated and installed in the diffuser of the wind tunnel. This fairing and the internal optics are depicted in Fig. 5. A small glass window on top allowed the laser sheet to enter the fairing. To prevent the buildup of seed material on the laser outlet window at the leading edge of this fairing, the glass is instead recessed within the fairing and no pressure seal is made. Instead, a constant buffer flow of filtered dry air is supplied to the fairing which exits the fairing counter to the primary wind tunnel flow through the same aperture as the laser sheet. In order to reduce the open area of this aperture and increase the momentum of the outgoing buffer flow, a 3D-printed nozzle is installed at this aperture. The required flow capacity of the complete buffer flow system and the aerodynamic design of the 3D-printed nozzle were thoroughly studied with CFD simulation to ensure adequate protection would be provided for the laser mirror. The mount for the final mirror was outfitted with a pair of piezoelectric actuators to allow for fine tuning of the sheet alignment with the facility without removing the fairing. The distance from the final mirror to the center of the measurement region was 1.2 m

The diffuser flowfield containing the opposing supersonic jets is highly turbulent and was found to generate noticeable beam steering in the laser sheet. To create a more benign environment, a particle diverter wedge assembly was installed in the preceding diffuser section which generated a wake region in which the laser sheet can propagate. This reduced the pressure required within the fairing as well. These wedges had the additional benefit of diverting a good portion of the

seed material away from the aperture of the laser mirror fairing. The assembly consists of a pair of 18° wedges (only one visible in Fig. 5 due to sectioning) mounted on a bar which allows for an adjustable gap to be set between them. This gap was set just large enough to allow the laser sheet to pass (~3 mm). The entire assembly was mounted to the facilty's standard probe traverse which allowed for the precise alignment of the gap and the laser sheet. While multiple axial stations are available on the mounting bar, the most forward position was used during this test entry.

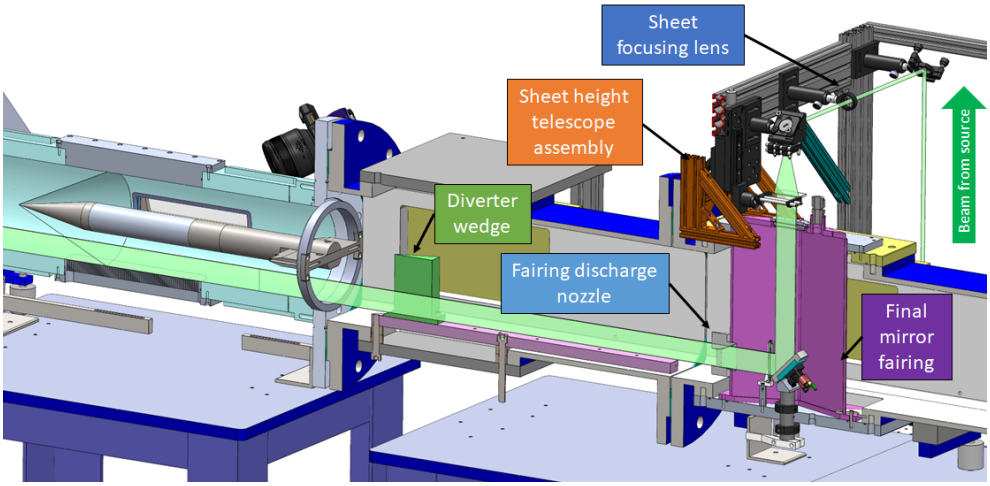


Fig. 5 Diagram of laser sheet routing into wind tunnel.

3. Imaging

Images were captured by a pair of interline-transfer CCD cameras (LaVision Imager SX6M) with pixel size of 4.54×4.54 µm and a resolution of 2752×2200. The stereoscopic pair were placed to capture back-scattered light at an approximate elevation angle of 22° and sweep angle of 45°. Off-the-shelf LaVision Scheimpflug mounts were used to tilt the camera sensor plane into alignment with the image plane of the laser sheet. Due to the compound tilt in viewing angle, careful rotation of the Scheimpflug tilt axis around the lens axis was required. Additionally, the camera sensor was rotated such that the axial extent of the field of view common to the two cameras was maximized. A bandpass filter (>93% transmission at 532 nm and 80 nm FWHM passband) was placed in front of each camera to minimize stray light from the test cell.

The cameras were calibrated using a 58 mm × 58 mm double-sided bi-level dot target (LaVision 058-5) which has a dot spacing of 5 mm and a level separation of 1 mm. The camera field of view relative to the test section was registered by placing the forward edge of this target coincident with the forward edge of the lower instrumentation window at $x = 406.4$ mm. A rendering of the camera arrangement used for 3-component (3C) velocity measurements is shown in Fig. 6 where the test section is configured for camera calibration.

All datasets used the same imaging distance and 100 mm lenses which resulted in an average pixel scaling of 65 $\frac{\text{pix}}{\text{mm}}$ and a dewarped common field of view as shown in Fig. 7. Here the two views are overlaid in world coordinates at the $z = 0$ plane. This trapezoidal field of view yields data relevant to the SWBLI investigation over a rectangular region measuring approximately 50 mm in x and 25 mm in $\overline{y}$ for each position of the translating system, which is shown by the red box in Fig. 7. As is clear from the figure, because the lower flow surface was removed when calibration images were captured, the target was able to be placed to extend below $\overline{y} = 0$, thus removing any influence of edge effects in the calibration equations in the region of interest.

While a polynomial mapping function was used for the calibration of the images for the computation of velocities, pinhole calibrations were also computed as a sanity check which yielded camera angles of $(42 \pm 1)°$ and $(22 \pm 1)°$ for the axial sweep and elevation angles, respectively. The target-based calibrations were performed each at the start of each test day. These calibrations were refined using the self-calibration procedures available in the LaVision software.

The breadboard supporting the camera assemblies was mounted to a screw-driven linear positioning stage and a pair of rails which were precisely aligned with the test section axis. By remotely actuating the stepper motor driving the screw, PIV data could be acquired at several axial stations without interrupting facility operation. Also, by virtue of the simple geometry of the viewing windows, the camera calibration should remain unchanged for any placement of the

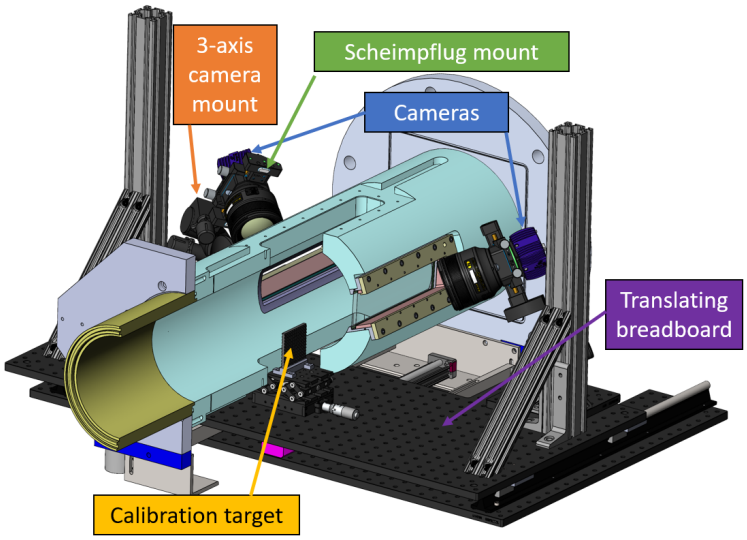
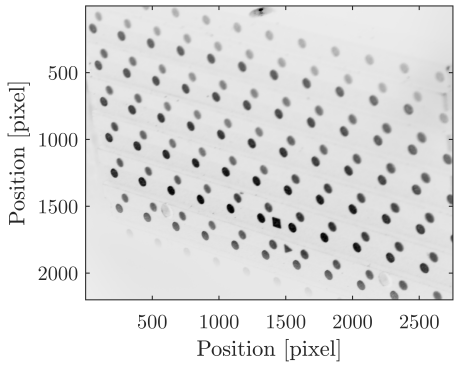
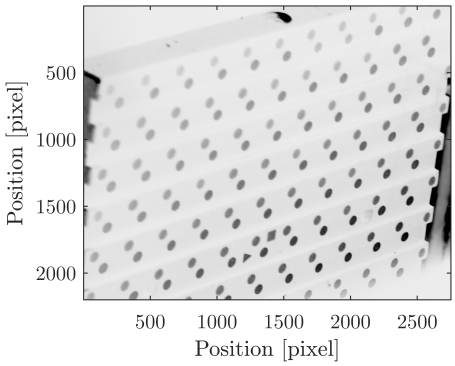


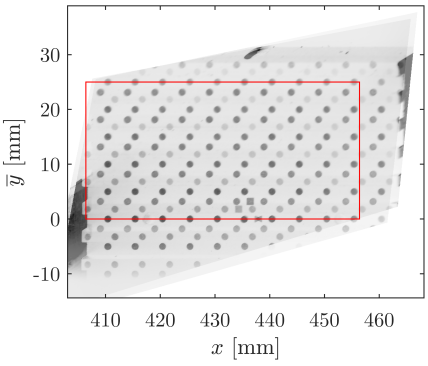
Fig. 6 PIV imaging layout for 3C measurements.



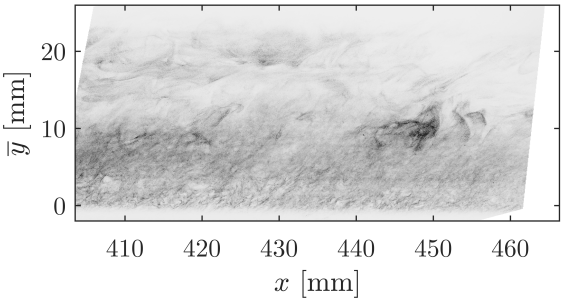
(a) Port camera calibration view.



(b) Starboard camera calibration view.



(c) Overlaid dewarped calibration images.



(d) Port camera sample particle image.

Fig. 7 Sample images for stereoscopic camera pair.

stage. The locations of these measurement regions and their overlap are shown in Fig. 8. This expedited data collection greatly by reducing the number of facility shutdown and restarts and also improved seeder performance by allowing the heating system to operate in steady-state rather than short bursts.

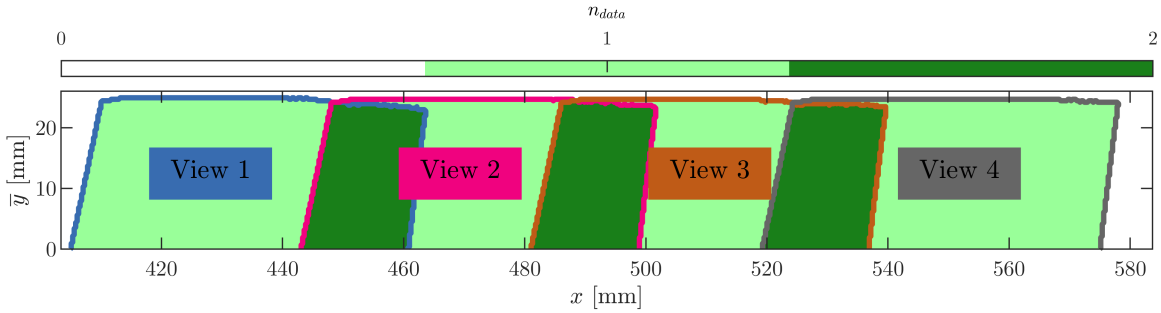


Fig. 8 Location and overlap of PIV measurement regions.

E. Test Parameters

The PIV data were obtained at several discrete camera positions which provided overlapping fields of view which spanned the region of interest in the axial direction. Each PIV data set covers a 50 mm × 25 mm region of the flow field. Translation between successive measurement stations was 38.1 mm, which yielded 24% overlap for stitching of the vector fields. The overall region sampled by PIV was x = 406.4–569.0 mm and $\overline{y}$ = 0–25 mm.

All PIV data sets were collected with a pulse separation time of 500 ns to resolve the low wall-normal and spanwise velocities. The PIV cross-correlation processing was performed with DaVis 10. An initial interrogation window size of 128 pix × 128 pix was applied with adaptive window weighting, which stretches the Gaussian-weighted windows in response to local velocity gradients detected in the prior pass. The windows were progressively reduced in size by half until the final window size of 32 pix × 32 pix was reached. Window overlap in the final pass was increased to 50% to increase vector density. For the selected pulse seperation time, the freestream particle displacement is 15% and 58% in the dewarped image coordinates for the initial and final window sizes, respectively. Spurious vectors were eliminated by applying a minimum peak ratio threshold and 5 passes of a spatial median filter. Typical processing time for a set of 1000 vector maps was 8 hours on a 24-core CPU.

A complete survey of the measurable test section region was made first with no model installed to characterize the baseline test section boundary layer. For these measurements, 1000 unique velocity fields were obtained for each camera position. For SWBLI datasets, ensembles of 1000 image pairs were again collected within and downstream of the shock interaction region, while 500 pairs were taken in regions upstream where the velocity should be identical to the baseline boundary layer measurements. Table 1 provides an overall summary of the breadth of SWBLI cases studied.

Previously reported results from probe and wall static pressure measurements showed that the offset distance did not have a large influence on the SWBLI behavior [8]. Therefore, to reduce the test matrix scope for the PIV measurements, only the $\ell = R/4$ offset was studied. This configuration provides for greater clearance between the region of interest and shock generator, thus reducing background scattering collected by the cameras. Additionally, the Reynolds number parameter space was consolidated to explore just the minimum and maximum cases for the two weaker shock configurations.

III. Results and Discussion

A large collection of PIV data has been collected and processed. The ensembles of instantaneous velocity field realizations are combined in both space and time to generate panoramic views of the mean and fluctuating velocity components across the entire SWBLI. To facilitate generation of matched CFD simulations to utilize this dataset, the inflow boundary layer was carefully characterized and key descriptive parameters are presented. Macroscopic views of the mean velocity and Reynolds stresses are also shown for comparison of the flowfield behavior under varying SWBLI strength in both axisymmetric and swept interactions.

In order to ensure that the test section modifications made to accommodate the PIV measurement technique did not

Table 1 Test matrix for PIV measurement campaign.

	$\alpha = 10°$			$\alpha = 13.5°$			$\alpha = 16°$		
θ \ Re_D	2×10^6	3×10^6	4×10^6	2×10^6	3×10^6	4×10^6	2×10^6	3×10^6	4×10^6
℄	✓		✓	✓		✓	✓	✓	✓
0°	✓		✓	✓		✓	✓	✓	✓
90°	✓		✓	✓		✓	✓	✓	✓
180°	✓		✓	✓		✓	✓	✓	✓

All PIV data on offset shock generator is at $\ell = R/4$.

significantly influence the SWBLI flowfield, comparisons were made between measurements made in the new PIV test section and the conventional version used for the probe measurement campaign. Figure 9 shows static pressure profiles in the two empty test sections operating at the bounding Reynolds number conditions for PIV testing. The data has been converted to an equivalent freestream Mach number (assuming no total pressure loss) to give context to the pressure values. The colored range of the conventional measurements shows the magnitude of variation from between the $\theta = 0°$ and 180° clock positions. The static pressures measured in the PIV test section were measured at both the $\theta = 0°$ and $\theta = 180°$ locations. The data from the modified test section agrees well with the conventional version over the region of interest to the SWBLI investigation, showing the same slow decay in Mach number as the test section wall boundary layer grows with downstream distance. Beyond a certain axial station ($x \approx 630$ mm at $Re_D = 2 \times 10^6$ and $x \approx 640$ mm at $Re_D = 4 \times 10^6$), the PIV test section does show a sharp reversal of the Mach number trend corresponding to the expansion that occurs due to the setback of the PIV viewing windows from the axisymmetric flow surface. However, the magnitude of this pressure rise is small (note the compressed scale of the ordinate) and is well downstream of the primary SWBLI of interest. This location provides the downstream bound for PIV data expected to match a truly axisymmetric test section.

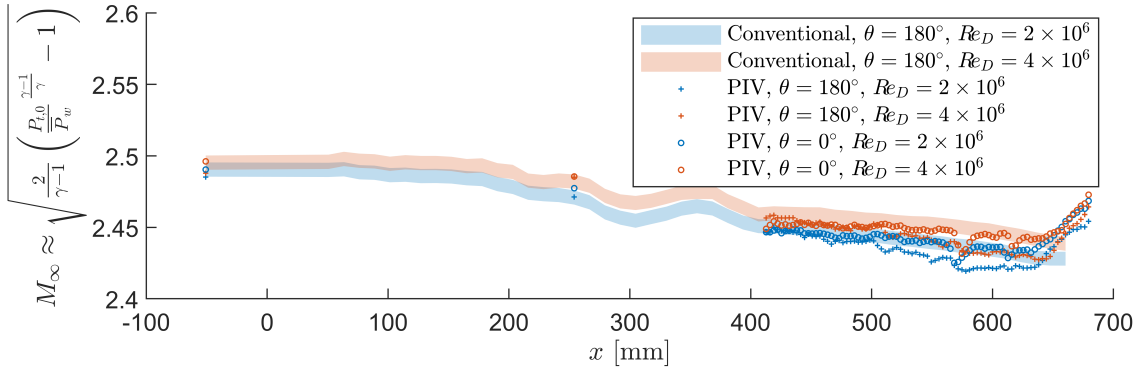


Fig. 9 Static pressure profiles in the PIV test section in comparison with conventional version.

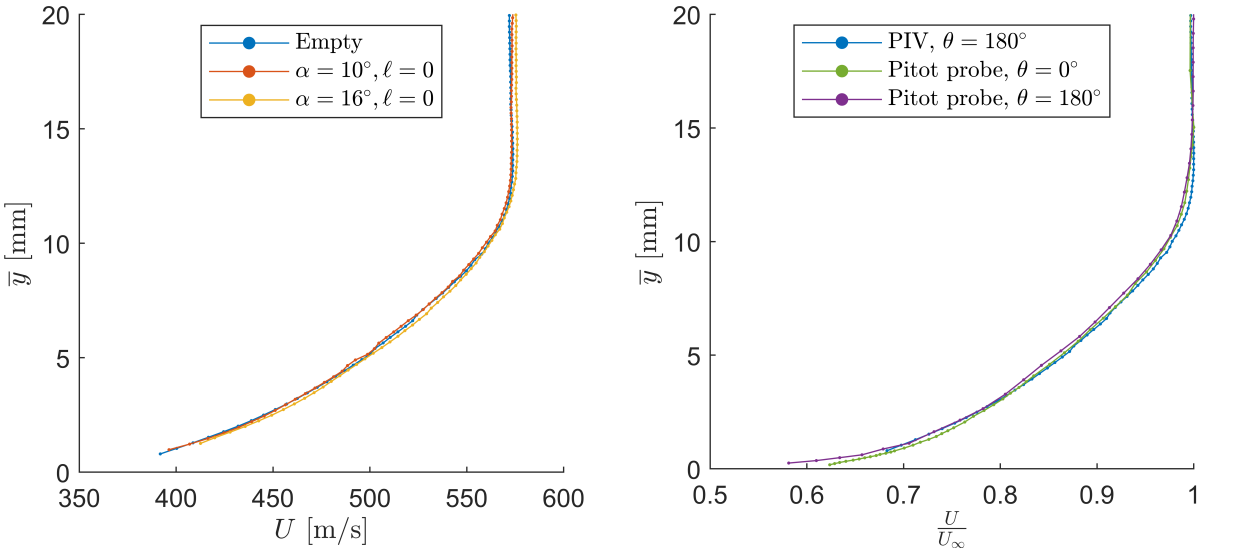
A. Inflow Characterization

Characterization of the incoming boundary layer was identified as a critical feature of a complete validation dataset. In the current test entry, the furthest upstream station accessible by PIV is at $x = 406.4$ mm. Due to reflections from the leading edge of the $\theta = 180°$ port appearing in the PIV image background, the incoming boundary layer profile was evaluated at $x = 419.1$ mm. This station is upstream of shock impingement for all shock generator configurations.

PIV measurements obtained at $x = 406.4$ mm for both an empty test section and with the shock generator installed are compared in Fig. 10a. Data are presented in dimensional units to directly compare the measured quantity, velocity. There is good agreement between the three examples shown despite the aero-optical effects introduced by the presence of the shock-expansion in the cases containing the shock generator. This is not surprising when considering the relatively

weak density changes generated in this flow.

The empty test section PIV data is also compared with Pitot probe data taken in the same test section in Fig. 10b. The probe data was acquired at both the $\theta = 0°$ and $\theta = 180°$planes for comparison. Data obtained at $\theta = 180°$ are measured in the identical location as the PIV, but require significant cantilever in the probe mounting apparatus. The $\theta = 0°$ require a less extreme mounting of the probe and thus improve positional accuracy. All 3 profiles show very good agreement within the boundary layer and also show a similar minor decrement in velocity just beyond the boundary layer edge, with the PIV profile being slightly more full near the edge. The reduction of the Pitot probe data necessitates an assumption of constant static pressure across the layer in the absence of a static pressure probe survey. Thus, a small variation in local static pressure near the boundary layer edge would only manifest in the PIV results which measure velocity directly. Otherwise, the similarity in boundary layer scale and velocity profile slope indicates that the integral parameters derived from PIV data should be in excellent agreement with equivalent values from probe measurements.



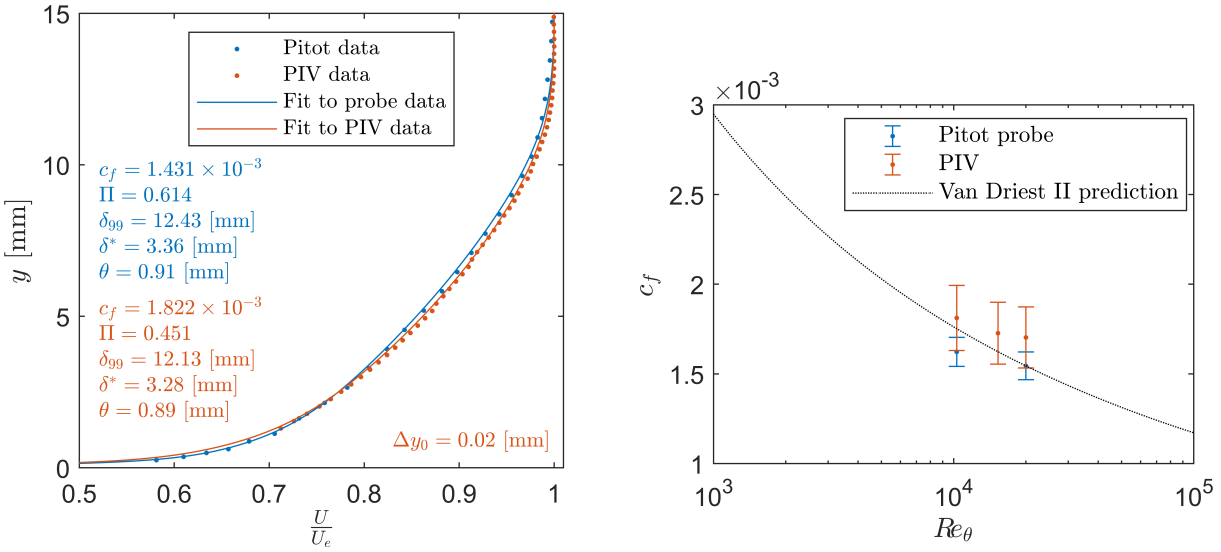
(a) PIV data in dimensional units.

(b) Comparison of PIV with probe measurements in empty test section.

Fig. 10 Sample incoming boundary layer mean velocity profiles at $Re_D = 2 \times 10^6$.

Fitting the incoming boundary layer profiles to a composite canonical turbulent boundary layer profile as described in Ref. 9 is challenging for this dataset. The extreme camera viewing angles required to avoid disturbing the SWBLI flowfield lead to a relatively large distance to the wall for the nearest PIV measurement. Additionally, the high Reynolds numbers and small scale of the test facility dictate that the viscous scale for the boundary layer is very small. This leads to boundary layer velocity profiles which only contain a few points within the logarithmic region. Consequently, the fitting routine faces an under-determined problem where many combinations of c_f, Π, and Δy_0 lead to similar levels of residual. This can result in PIV velocity profiles which look similar to the Pitot probe data, but have very different parameters resulting from a global "best-fit". This is illustrated in Fig. 11a where the optimal c_f value from the PIV data is 27% higher than that of the Pitot data while the overall profile and scale parameters are a near match (δ_{99} being the most affected due to its high sensitivity to the velocity profile slope at the boundary layer edge). While the friction coefficient from the PIV data is higher than the expected value in this Reynolds number range, the wake parameter is more in line with what is expected for the slight adverse pressure gradient in the constant-area test section ($\Pi = 0.55$ for zero pressure gradient). The problem of sparse data in the logarithmic region is only exacerbated at higher Reynolds numbers where the boundary layer scale is reduced. The presence of many solutions near the global optimum can be seen by constraining the fit of the PIV data to match the c_f of the Pitot profile. This yields a best-fit solution which closely matches all parameters of the Pitot profile with a concurrent increase of 16% in the total residual error. However, this result will not be obtained organically without a priori knowledge of the skin friction and manual constraints. With this uncertainty in the skin friction acknowledged, future users of this data as a CFD validation dataset are encouraged to match the velocity profile (or at least integral parameters) rather than a skin friction coefficient shown herein.

In the process of fitting the boundary layer data with canonical log-law profiles, the von Kármán constant, κ, is a key parameter. Because the composite formulation used to define the canonical boundary layer profile incorporates the buffer layer overshoot correction of Monkewitz et al. [10], the value reported therein ($\kappa = 0.384$) was used for the fit. This value has been shown to be the optimal value for zero pressure gradient turbulent boundary layers [11]. If the traditional value of $\kappa = 0.41$ is used, the c_f for each of the profiles is increased by 14% which is proportional to the square of the increase in κ, as expected. The wake parameter and boundary layer scale parameters are unaffected.



(a) Fit of empty test section data at $Re_D = 2 \times 10^6$ to canonical turbulent boundary layer profile.

(b) Comparison of measured incoming boundary layer c_f against predictions by the van Driest II transformation.

Fig. 11 Incoming boundary layer profile parameter evaluation.

The Sun & Childs method [12] was also applied to this profile to analyze the profiles in a fashion consistent with the probe data previously presented [7]. This method should recover parameter values very near those obtained from the composite log-law profile with the notable exception the wake parameter. The Sun & Childs method uses Coles' sinusoidal wake function which was shown by the author of the wake function used in the composite profile to be deficient in modeling the velocity near the boundary layer edge [13]. The Sun & Childs method yields values for c_f which are 2% and 10% higher than the composite log-law method for the PIV and probe data, respectively, when using a matching $\kappa = 0.41$ value.

The boundary layer fitting procedure depicted in Fig. 11a was applied at all three Reynolds number conditions to quantify the incoming profile for CFD simulation. The results are summarized in Table 2. The values based on integral parameters should be favored when setting up simulations due to the relatively higher uncertainty in determining the friction coefficient. Figure 11b presents the computed skin friction values against the Kármán-Schoenherr incompressible flat plate turbulent boundary layer correlation with the van Driest II transformation, as suggested in Ref. 14. The data are all within 6% of the correlation and show the correct trend, indicating the transverse curvature of the wall has little effect on the skin friction as expected for $\frac{\theta}{R} \ll 1$ [15].

Table 2 Incoming boundary layer conditions.

Re_D (nominal)	M_0	Re_θ	Re_{δ_2}	$\frac{x_1 - x_i}{\delta_{99}}$	c_f	Π	Re_τ
2×10^6	2.49 ± 0.01	10,500	5,730	-6.8 to -5.8	1.81×10^{-3}	0.453	2.02×10^3
3×10^6	2.50 ± 0.01	15,200	8,260	-7.0 to -5.9	1.73×10^{-3}	0.472	2.84×10^3
4×10^6	2.50 ± 0.01	19,100	10,200	-7.1 to -6.0	1.70×10^{-3}	0.397	3.69×10^3

Turbulence in the incoming boundary layer is also critical information for matching CFD inflow conditions to the

test. With the hot-wire probe measurements, a significant data reduction effort is required to extract a pure velocity measurement from the measured signal which is sensitive to $(\rho u)'$, T_t', and their cross-correlation (see Ref. 7 for details of data reduction). PIV, on the other hand, directly measures the flow velocity, but extracts no information about density fluctuations. Weighting the stress values by the local mean density (Morkovin scaling [16]) has been shown to remove influence of the compressibility [17]. In order to perform Morkovin scaling, a local density through the boundary layer was computed based on the measured mean axial velocity and the Walz relation [18],

$$T = T_w + (T_r - T_w)\left(\frac{\overline{u}}{\overline{u}_\infty}\right) + (T_\infty - T_r)\left(\frac{\overline{u}}{\overline{u}_\infty}\right)^2 \tag{1}$$

which is simplified in the current experiment due to the facility being controlled such that $T_w = T_r$.

In Fig. 12, profiles of the incoming root-mean-square (r.m.s.) axial velocity fluctuations are compared. Acknowledging the difference in wall roughness (conventional test section was machined to ≤ 8.1 µm average surface deviation while the PIV test section was painted black and sanded to an unspecified finish), the profiles show modest agreement in general character. The enhanced level of turbulence exhibited by the PIV profile is likely due to the higher noise in the measurement. The PIV apparatus is limited by a finite level of random error which is driven by the ability of the cross-correlation method to accurately determine the fluid displacement, the stereoscopic reconstruction accuracy, and the precision of the timing equipment. These factors combine to set the noise floor of the measurement. The freestream flow, in particular, is a region where the hot-wire provides a more accurate measurement due to its lower noise floor. As will be discussed further in Section III.D, the stereoscopic reconstruction error is non-negligible relative to the weak turbulent fluctuations in the freestream. Moving toward the wall, both profiles exhibit the expected monotonic increase in turbulence intensity with the PIV showing distinctly higher values throughout the boundary layer. As with the freestream region, the PIV measurement configuration used in this test was incapable of accurately resolving this low level of turbulence. Within the boundary layer, the effect of in-plane mean velocity gradient becomes non-negligible and diminishes the correlation peak amplitude, introducing random noise into the measurement [19].

As a comparison for the expected magnitude of these profiles, the peak u'^{+}_{rms} value should be around 3 for a flat plate incompressible turbulent boundary layer at this Reynolds number [20] (flat plate data is used for rough comparison since the thin boundary layer relative to the test section radius makes this flow more like a 2D boundary layer than fully-developed pipe flow). However, peak turbulence intensity occurs nearer to the wall than either measurement presented here was able to probe. This peak has been observed to occur in the buffer layer around $y^+ = 15$ which corresponds to 64 µm and 120 µm at the lowest and highest Reynolds numbers of the current experiment, respectively. Thus, the data presented here should fall below this expected maximum value since they are confined to the logarithmic region and beyond. The PIV measurement, in particular, is ill-suited to make measurements deep into the layer due to the camera viewing angles necessitated by the test section geometry. For the logarithmic region of the layer, analytical predictions using the attached-eddy model imply that u'^{+}_{rms} should peak at 2.0 [21]. This falls between the peak magnitude of the two measurements shown here. Further refinement of the data analysis methods are planned to investigate this small discrepancy and quantify the error associated with each measurement.

As discussed, the stereoscopic PIV measurement is able to obtain all 3 components of velocity. Thus, all 6 of the kinematic turbulent stress terms can be computed (representative of the Reynolds shear stress if density fluctuations are considered negligible). These stress values are plotted in Fig. 13 as a function of wall distance.

In Fig. 13a, the PIV data appear to generally follow the expected behavior for boundary layer turbulence in the outer region, where the intensity monotonically increases toward the wall in the streamwise component and the spanwise and wall-normal quantities are approximately 60% and 40% of the streamwise value, respectively [22–24]. As discussed, the magnitude of the axial fluctuations are in line with expectation for the region beyond the buffer layer at $Re_D = 2\times10^6$ and the maximum value should should increase mildly with Reynolds number. The empirical prediction for the wall-normal fluctuation profile in turbulent boundary layers predicts a peak value of 1.18 at $\frac{\overline{y}}{\delta} = 0.14$ for the $Re_D = 2\times10^6$ case, which is appreciably higher than what is observed in the PIV profile [25]. There, the peak value of 0.97 occurs further from the wall ($\frac{\overline{y}}{\delta} = 0.40$) and the value at $\frac{\overline{y}}{\delta} = 0.14$ is only 0.85. All 3 normal components show an elevated magnitude at the boundary layer edge, which is indicative of the PIV measurement noise floor which was previously discussed. The magnitude of this discrepancy is emphasized here by the local density scaling as well. The high freestream density relative to the wall ($\rho_\infty/\rho_w = 2$) enhances the stress values. The shear stresses are presented in Fig. 13b, where the primary shear is in $\overline{u'v'}$ and the other two components are near zero, as expected. The non-zero shear in the freestream is again an artifact of the density scaling. As with $\overline{v'v'}$, the maximum measured shear stress values are noticeably lower than the expectation for a flat plate boundary layer in this Reynolds number range ($-\frac{\rho}{\rho_w}\frac{\overline{u'v'}}{u_\tau^2} \approx 0.93$–$0.95$ at $\frac{\overline{y}}{\delta} \approx 0.03$)

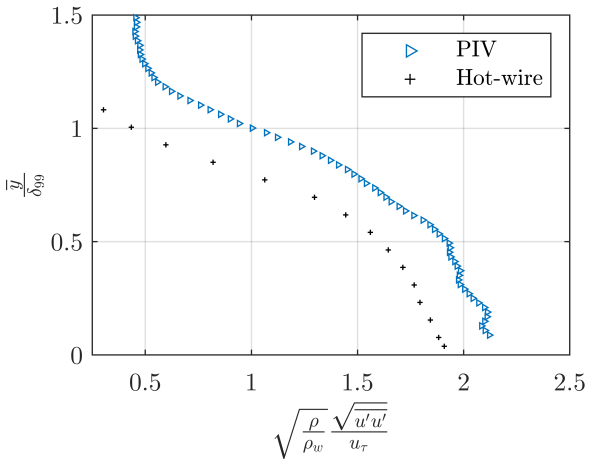
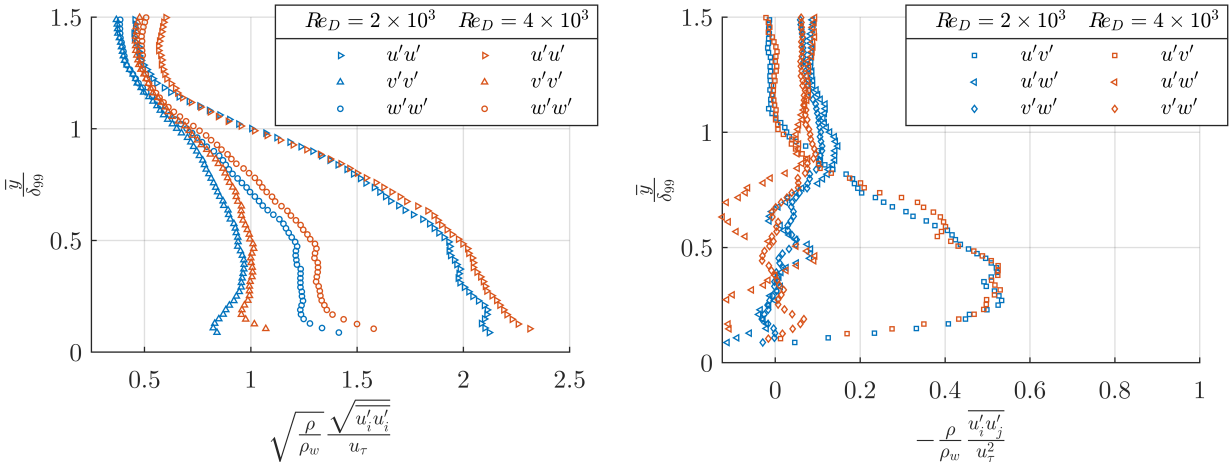


Fig. 12 Incoming boundary layer streamwise turbulence intensity profile at $Re_D = 2 \times 10^6$ compared to hot-wire measurements.

[26]. The PIV measurement departs further from the expected behavior by decreasing for $\frac{\overline{y}}{\delta} \leq 0.4$. This observation is consistent with other particle-based measurements made in compressible turbulent boundary layers [27–29].



(a) Normal components. **(b) Shear components.**

Fig. 13 Morkovin scaled incoming boundary layer turbulent stress profiles at $Re_D = 2 \times 10^6$ and 4×10^6.

While direct causation of the suppressed peak shear is difficult to isolate, there are a few candidates, primarily seed particle inertia, finite spatial resolution of the technique, and optical distortion. The suppression of wall-normal stress in both LDV [27] and PIV [28, 29] measurements has been previously noted in supersonic turbulent boundary layers. In Ref. 27, low-pass filtering of the turbulence spectra due to the finite inertia of the tracer particles was found to cause the observed reduction in fluctuation magnitude. In the PIV measurements of Ref. 29, the combination of spatial averaging due to the finite interrogation window size and particle inertia were found to act similarly. Both works attributed the greater sensitivity of the wall-normal fluctuations to the flatter power spectrum containing more energy at scales smaller than the measurement cutoff. Recently, investigation of the PIV spatial resolution effects were made using Mach 5 turbulent boundary layer DNS data and synthetic images [30]. The inherent dilemma of minimizing PIV interrogation window size while controlling spurious correlations was illustrated.

The effect of seed particle inertia can be investigated by comparing the behavior of the turbulent stresses at the two Reynolds number conditions. The inner-normalized peak shear stress, $\overline{u'v'}/u_\tau^2$, should be relatively invariant with

Reynolds number in a flat plate turbulent boundary layer where $Re_\tau > 1000$ [26, 31]. The similarity of the shear stress profile for the two Reynolds numbers presented in Fig. 13b reflects this behavior. However, because attenuation of small-scale turbulence should worsen with increasing Reynolds number for a fixed measurement resolution, the spatial averaging inherent to PIV cross-correlation is likely being balanced by another aspect of the measurement which causes an opposing effect. It is hypothesized that the measured turbulence intensity is reduced in the PIV results at the lower Reynolds number due to non-continuum effects in the seed particle drag. Velocity fluctuations which are smaller in magnitude are more susceptible to these effects [9, 32].

The variation of local seed particle drag through the boundary layer is shown in Fig. 14, where the local drag coefficient is estimated using the Loth spherical particle drag model [33] and normalized by Stokes' solution for creeping flow around a sphere. A particle diameter of 0.8 µm was used, which matches the median particle size observed in Ref. 9. In this estimate, a profile of the estimated velocity fluctuations is constructed which generally follows the $\frac{\sqrt{\overline{u'u'}}}{\overline{U}}$ profile in Fig. 12 by linearly varying u_{rms} from 1% in the freestream to 15% at the wall. Several multiples of this r.m.s. fluctuation value are shown to represent varying levels of fluctuation strength. It is important to note that there is an "area under the curve" inherent to these plots where the turbulent fluctuations which are smaller in magnitude exhibit a unique response function which is always reduced from that of stronger fluctuations. This can lead to the effect seen in Fig. 13 if a large portion of the turbulent fluctuations are small in magnitude. For example, if the turbulent fluctuations were normally-distributed, then 68.3% of fluctuations are to the left of the first curve, 95.5% are below the second, and 99.7% are contained by the third. Additionally, the rough magnitude of fluctuating velocity in other components are significantly lower than $\overline{u'u'}$ and thus would show a reduced drag coefficient.

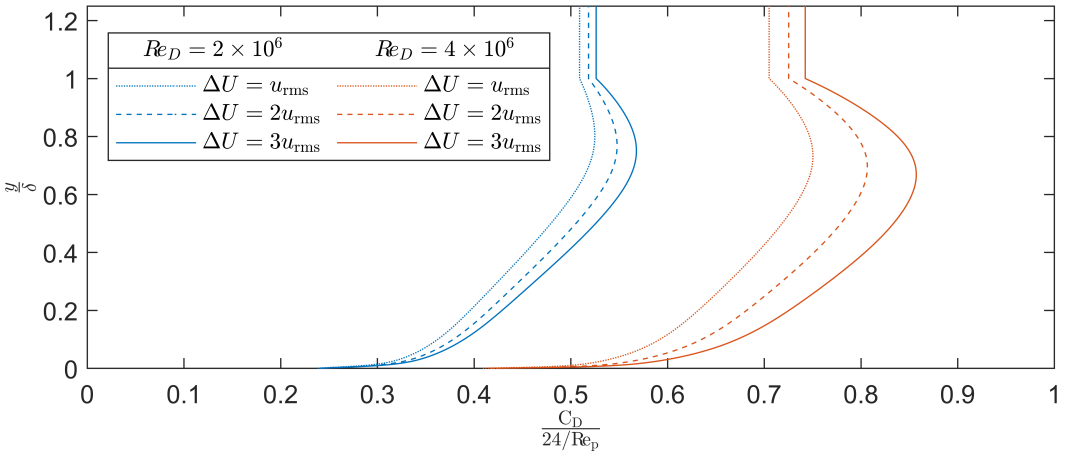


Fig. 14 Local particle drag coefficient estimates through boundary layer profiles [33].

It is clear that the higher Reynolds number case shows greater particle drag coefficient values and thus would be expected to exhibit more faithful tracking of the underlying gas flow by the seed particles which are imaged by the PIV system. In both cases, the particle drag is expected to be reduced from the classical Stokes value due to rarefaction. In Ref. 9, the post-shock measurements made to assess seed particle inertia were located in a flowfield dominated by the large velocity change across the shock wave and the relatively high density gas in the post-shock regime ($Kn \leq 10^{-2}$). This is not a flaw in the shock response methodology, as the obtained particle diameters are accurate, but rather an inherent issue in measuring small velocity fluctuations in rarefied gas flows with the PIV technique.

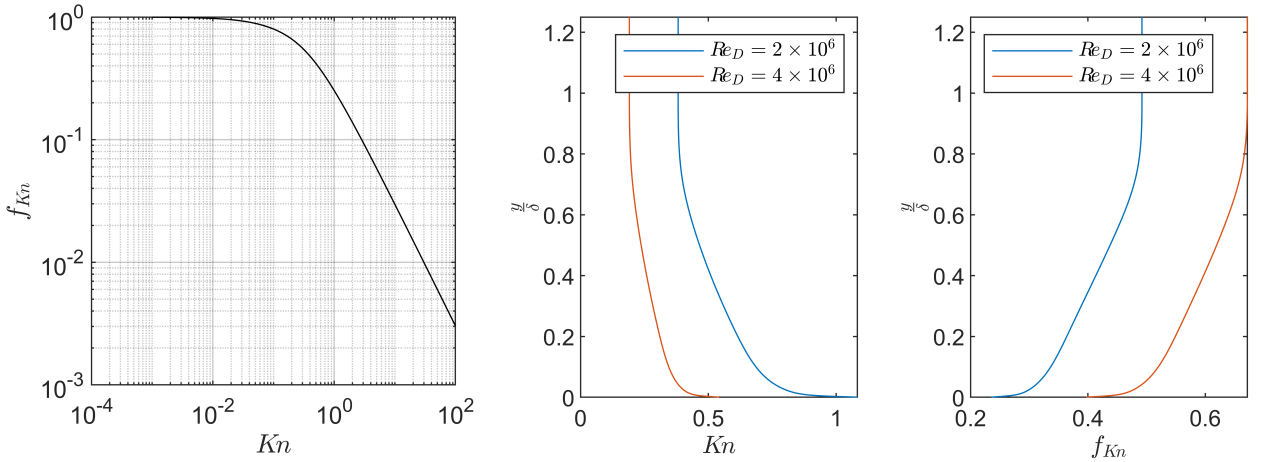
Non-continuum effects are accounted for in the Loth model through the Cunningham correction factor [34]

$$f_{Kn} \equiv \frac{c_D(Kn \gtrapprox 10^{-2}, Re_p)}{c_D(Kn \to 0, Re_p)} = \frac{1}{1 + Kn\left(2.514 + 0.8e^{-.055/Kn}\right)} \tag{2}$$

The magnitude of this factor is plotted in Fig. 15a. For $Kn \lessapprox 0.01$, the value becomes nearly unity and the gas rarefaction has little effect on the particle drag. For larger values of Kn, the particle drag is significantly reduced, falling to 0.25 at $Kn = 1$. The Knudsen number, which is exactly inversely proportional to Re_D in the current experiment where T_t and M_∞ are held constant, is plotted through the best-fit composite velocity boundary layer profiles for the bounding

Reynolds number cases in Fig. 15b. Combining the results shown in these two plots, profiles of the Cunningham correction factor can be evaluated as shown in Fig. 15c. These profiles are purely a function of the local gas density, which continually decreases as the wall is approached for the adiabatic wall condition in the current experiment. Comparing these profiles to Fig. 14, it is clear that nearly all of the local particle drag suppression in the boundary layer is attributable to non-continuum effects.

The unfortunate takeaway from this analysis is that the competing effects of finite spatial resolution and seed particle inertia result in no discernible trend for better measurement accuracy at a particular Reynolds number. Attempts to correct the PIV data for particle inertia effects are infeasible due to the unknown true Reynolds stress spectra for a compressible turbulent boundary layer at this Reynolds number and the complexity in determining an accurate correction at each spatial location. Polydispersity (non-uniformity in size) of the seed particles adds an additional layer of complication (Fig. 14 are computed for a single particle size) as particle response to the same gas acceleration varies non-linearly with scale. Thus, the turbulent quantities presented in this work are given directly with the acknowledgment that the ultimate magnitude is suppressed somewhat near the wall by non-continuum effects. All effort was made to minimize these effects by using a low-density seed material and generating the smallest droplets possible. Similarly, the spatial resolution in PIV measurements is limited by the interrogation window size used when cross-correlating the image pairs. The minimum size for these windows is typically limited by the concentration of seed material in the flow. In the current experiment, the seeding system was operated in such a way that it provided the maximum seed particle concentration without increasing the size of the droplets. This resulted in a seed concentration which was amenable to PIV processing with a 32×32 final window size. A potential future endeavor to improve upon the spatial resolution of the current dataset could investigate seeding system modifications or clever image processing techniques. However, a further reduction in window size would likely necessitate a reduction in the scope of data collection due to the increase in computational cost to process the data. In this manuscript, the minimum Reynolds number experimentally available will be prioritized for analysis to make the flowfield computationally tractable for fully-resolved large eddy simulation (LES), which already strains the current sate of the art [35].



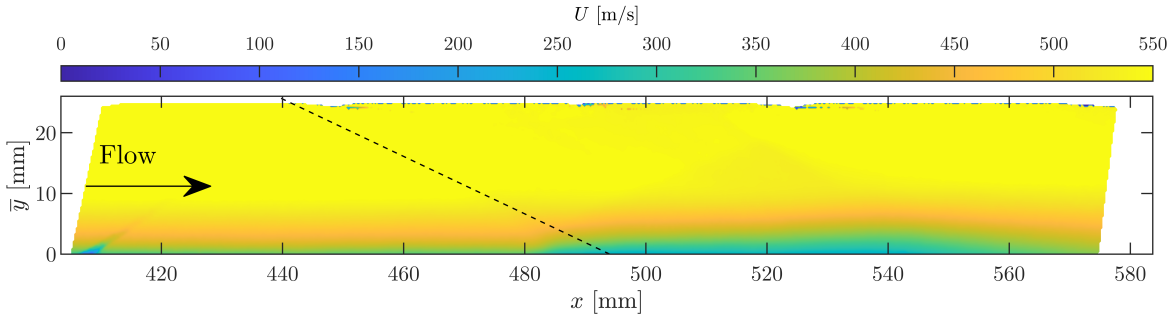
(a) Cunningham correction factor (f_{Kn}) as a function of Kn. [33] **(b) Local Kn through boundary layer.** **(c) Local f_{Kn} through boundary layer.**

Fig. 15 Estimates of non-continuum flow effects on the particle turbulence response within the incoming boundary layer.

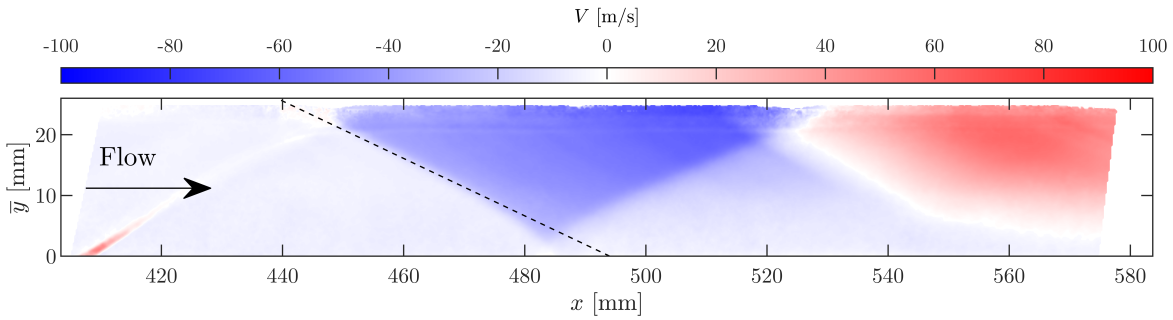
B. Axisymmetric Interactions

With the shock generator aligned coaxially with the test section ($\ell = 0$), an axisymmetric SWBLI is generated. Figure 16 shows a global view of the velocity field for the $\alpha = 10^\circ$ axisymmetric interaction at $Re_D = 2 \times 10^6$. Ensembles of velocity data at each camera position were flattened to mean values and then stitched together using a linear blending in the overlapping spatial regions. The W component is omitted for brevity as it is insignificant for this two-dimensional flowfield (measured values are $\pm 20 \frac{\text{m}}{\text{s}}$ across the entire field). Previous testing has shown the pressure rise in this

interaction to be insufficient for separation [8]. However, a definitive thickening of the boundary layer can be observed in the U field due to the adverse gradient at the impingement location. The influence of the shock wave upstream of the inviscid trace (dashed line) can be seen in both the U and V fields within the boundary layer. It is also important to note that the region downstream of the shock is also influenced by the expansion fan emanating from the shoulder of the cone-cylinder. The effect is hardly discernible in Fig. 16, but will become apparent in stronger interactions.



(a) Axial velocity, U.



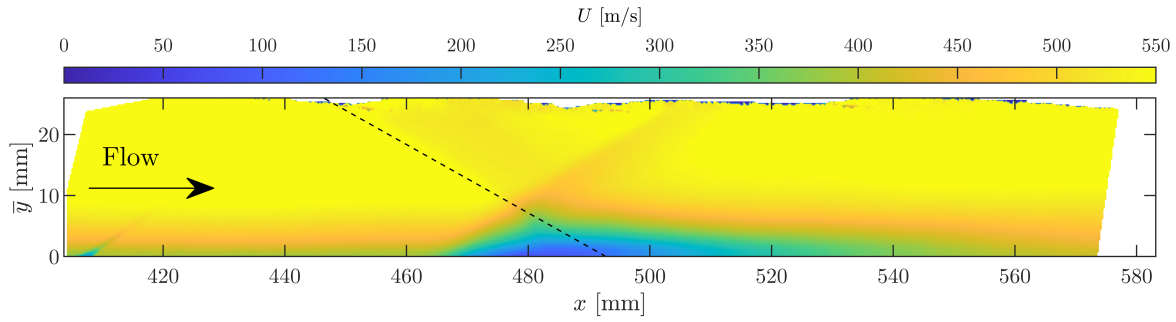
(b) Wall-normal velocity, V.

Fig. 16 Compilation of PIV mean velocity data for the $\alpha = 10°$, $\ell = 0$ interaction at $Re_D = 2 \times 10^6$.

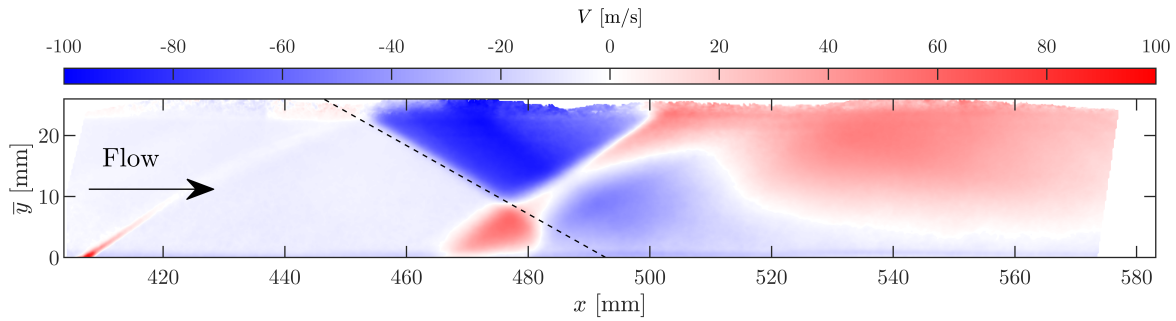
Figure 17 shows a similar compilation of the mean velocity fields for the $\alpha = 16°$ axisymmetric interaction at the same Reynolds number. Here, the stronger impinging shock separates the boundary layer [8]. As expected, the upstream influence of this stronger shock is greater as well, beginning at $x \approx 460$ mm. The boundary layer appears to thin more rapidly after the flow has reattached downstream of the interaction than in the $\alpha = 10°$, primarily due to the stronger expansion emanating from the shoulder of the cone-cylinder. The forward shift of the expansion fan toward initial shock is also apparent in the V field, resulting in a decrease in compression length at the wall, which was analyzed in detail in Ref. 8.

In Fig. 18, velocity data were extracted from the fields shown in Figs. 16 and 17 at select stations to make direct comparisons between the two interactions. This figure shows quantitatively how the stronger impinging wave retards the near-wall velocity to nearly zero while the other case drops only to 50% of the freestream value. The $\alpha = 16°$ interaction also shows a more rapid recovery of the profile due to the upstream shift in the influence of the expansion emanating from the shoulder of the cone-cylinder. A local estimate of the precision at which the ensemble of PIV data estimates the mean velocity value is quantified by the horizontal error bars, which represent a 99.7% of the standard error of the mean. This estimate does not incorporate errors which may be introduced by the PIV technique (which will be discussed in Section III.D), but simply provides an indication of how the relatively large number of PIV images averages out any effect of the random sampling of the turbulent velocity field.

The turbulent stresses of interest are presented for the $\alpha = 16°$ case in Fig. 19 below. Data from the various camera views was blended using the same method as the mean velocity data. The $\overline{u'u'}$ field peaks in the shear layer above the separation bubble. The wall-normal height of peak intensity grows with downstream distance until it reaches the inviscid impingement line. Close inspection of this line of peak intensity shows its origin to be just downstream of the mean location of the reflected shock foot. This region of high axial turbulence rapidly decays downstream of the



(a) Axial velocity, U.



(b) Wall-normal velocity, V.

Fig. 17 Compilation of PIV mean velocity data for the $\alpha = 16°$, $\ell = 0$ interaction at $Re_D = 2 \times 10^6$.

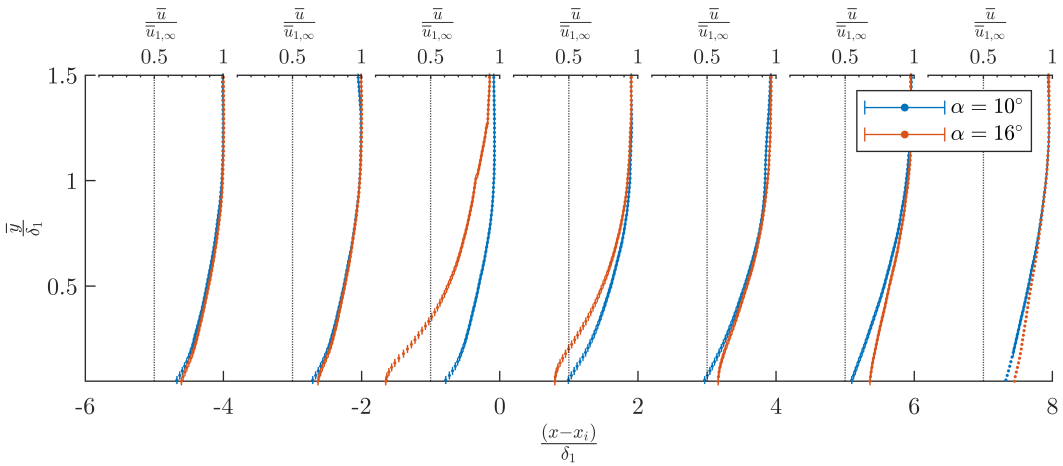


Fig. 18 Profiles of axial mean velocity at select stations through the $\alpha = 10°$ and $16°$ axisymmetric interactions at $Re_D = 2 \times 10^6$. *Dashed lines indicate the sampling station (lower abscissa). Error bars indicate 3 times the local standard error of the mean.*

interaction. The shear stress field, on the other hand, is dominated by non-vortical turbulence originating from reflected shock oscillations which dwarf the true shear turbulence generated within the interaction. This is due to the large jump in post-shock wall-normal velocity relative to the upstream value. Oscillation in the shock position leads to velocity field instances where v' can achieve large magnitude simply due to excursions from the mean shock position. This is nearly impossible to remove from the PIV data, as accurately identifying the instantaneous reflected shock position within the turbulent velocity field is impossible. Downstream of the reflected shock foot, there appears to be a reversal in the sign of the kinematic shear stress from negative (slow-moving fluid transported away from the wall or fast-moving fluid toward) to slightly positive. This has also been observed in PIV data obtained in a Mach 2.1 planar impinging shock interaction [36]. Downstream of the interaction, the naturally-occurring negative shear stress begins to dominate and shows a gradual equilibration with streamwise distance. The $\overline{v'v'}$ field is similarly dominated outside of the interaction by reflected shock motion artifacts while the post-shock boundary layer looks qualitatively similar to the shear stress distribution. The intensity in this component is seen to recover more slowly than the axial. The out-of-plane turbulence, $\overline{w'w'}$, shows a distinct rise behind the reflected shock foot which dissipates quite slowly with downstream distance. The increase in background magnitude for both of these stresses near the top of the measurement region above the reflected shock is partially driven by statistical noise from reduced number of valid vectors in that region. While the rest of the fields shown have 92–95% yield throughout, that particular region suffered from a lack of seeding and thus contains approximately valid measurements in 60% of the 1000 vector maps. As with the mean velocity, only the components in the x-y plane are significant and thus $\overline{u'w'}$, $\overline{v'w'}$, and $\overline{w'w'}$ are omitted for brevity.

In contrast, the velocity fluctuation components for the $\alpha = 10^\circ$ interaction are shown in Fig. 20. The color scale limits were maintained at the values from Fig. 19 for ease of comparison. It is clear that this unseparated interaction induces only a slight increase to the turbulence intensity from the baseline level present in the incoming boundary layer. The reflected shock in this case shows very little motion; thus, the shock position is not highlighted by a region of artificially high shear or wall-normal intensity.

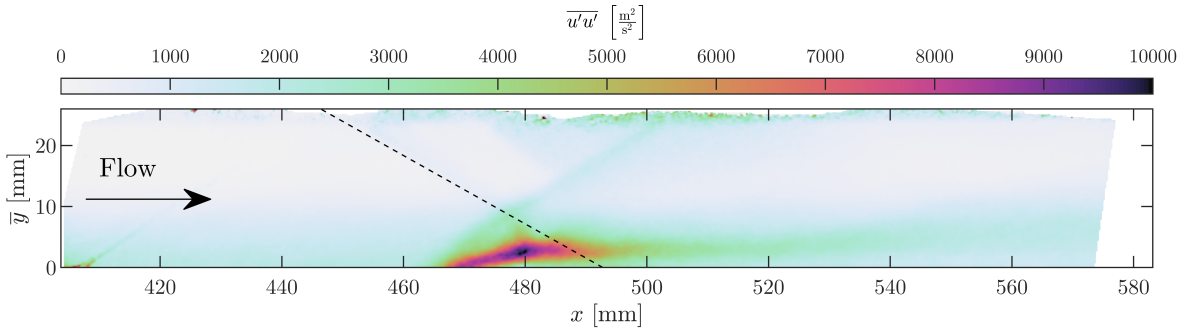
Figure 21 compares the profiles of select turbulence intensity components between the interactions of different strength. All of the profiles match well in the undisturbed upstream boundary layer, as they should, and also all recover to similar behavior beyond $6\delta_1$ downstream of the inviscid impingement point. Within the interaction region, there are significant differences between the two cases. These plots also give context to the overall r.m.s. turbulence levels relative to the freestream velocity.

In the axial component, the separated interaction profiles show the initial increase in the near-wall region which moves gradually away from the wall and decreases in intensity with downstream distance. There is also a slight enhancement ($0.04\bar{u}_{1,\infty}$) at the inviscid impingement station outside of the boundary layer due to motion of the reflected shock. The $\overline{u'v'}$ profiles show the strong shear generated on top of the separated region in the $\frac{x-x_i}{\delta_1} = -2$ profile which is completely absent in the unseparated interaction. The post-interaction profiles also show a peak in shearing which moves away from the wall with downstream distance, appearing to originate from the inviscid impingement station. In the profiles immediately downstream of the interaction, this peak is much more dramatic in the separated case, but is also present in the unseparated data. At the furthest downstream station shown, the shear stress profiles have evolved to nearly identical behavior which still contains significant enhancement over the undisturbed inflow profile. As with the axial intensity, the spanwise fluctuations for the separated interaction are increased in two distinct zones: one within the boundary layer which is associated with and one further from the wall which is associated with the reflected shock motion (and statistical noise due to low vector yield). While the variations within Figs. 19c, 19d, 20c and 20d appear to be dramatic, this is due to the selection of a tight color scale to enhance contrast. In practice, the variation within these components is quite subtle, even for the separated case. The maximum increase in $\sqrt{\overline{w'^2}}$ over the inflow profile is a 50% enhancement which occurs in the shear layer atop the separation zone. At the furthest downstream station shown, the profile has relaxed to within 20% of the incoming boundary layer in the near-wall region with an enhancement of the root-mean-square by 10–20% of $\bar{u}_{1,\infty}$ through the rest of the profile. The unseparated case, in contrast, shows a gradual increase in peak intensity with distance downstream of the interaction and an overall expansion away from the wall concurrent with the overall thickening of the boundary layer seen in Fig. 16a.

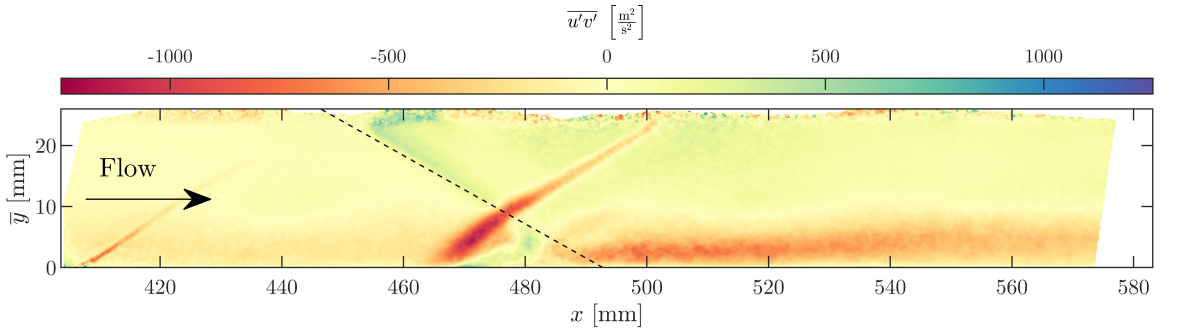
In this flowfield, the production of normal turbulence components,

$$P_{ii} = -2\overline{u_i'u_j'}\frac{\partial \overline{U_i}}{\partial x_j}, \tag{3}$$

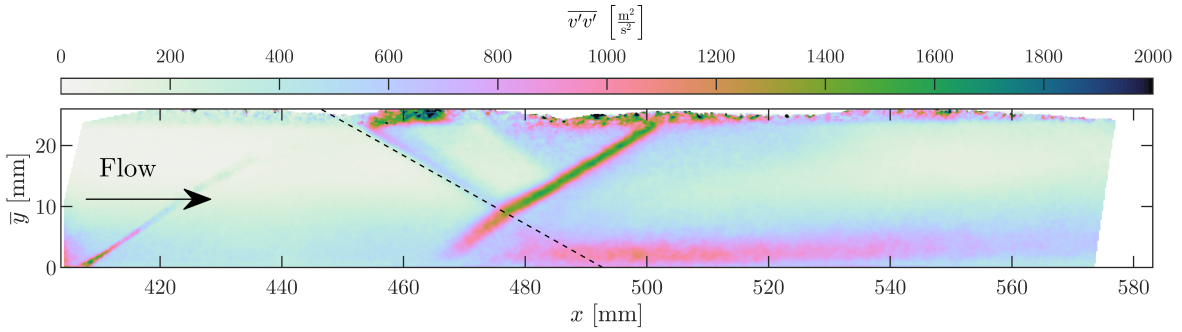
can be simplified by the assumption of minimal out-of-plane velocity gradient. Thus, the production depends only on terms which were measured with PIV. Figure 22 shows the streamwise turbulence production field, which is dominated



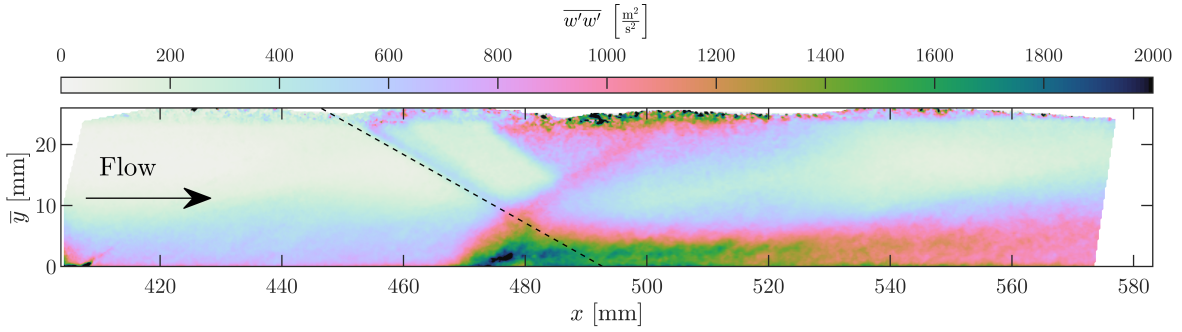
(a) Axial turbulence intensity, $\overline{u'u'}$.



(b) x-y plane shear stress, $\overline{u'v'}$.

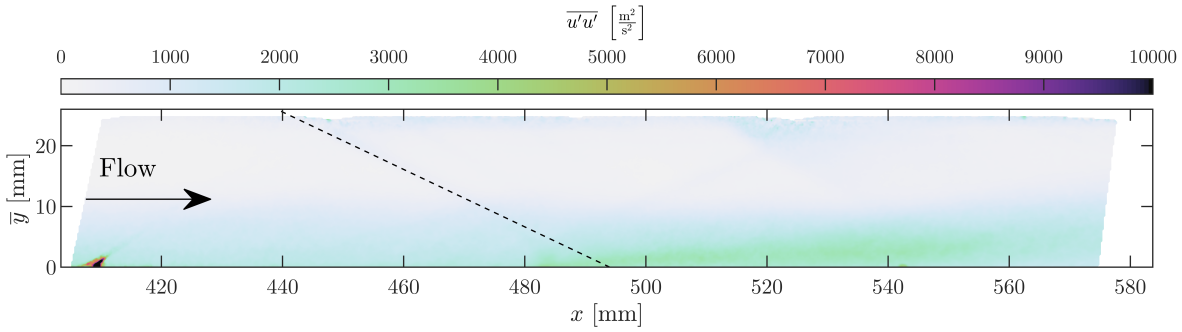


(c) Wall-normal turbulence intensity, $\overline{v'v'}$.

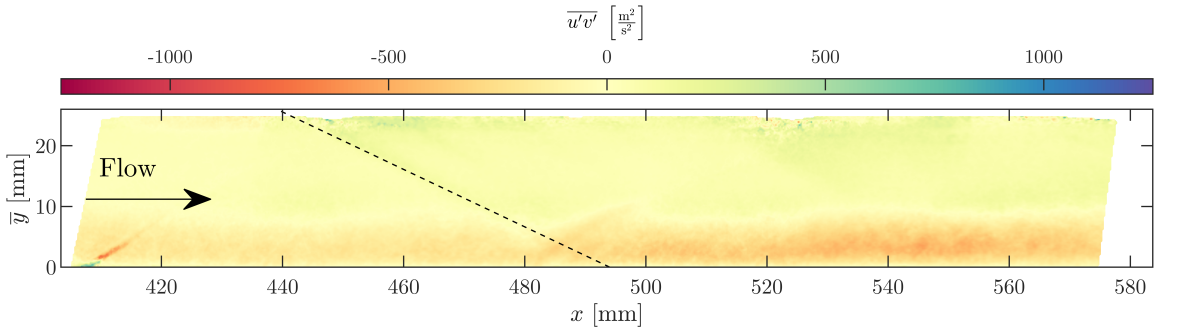


(d) Spanwise turbulence intensity, $\overline{w'w'}$.

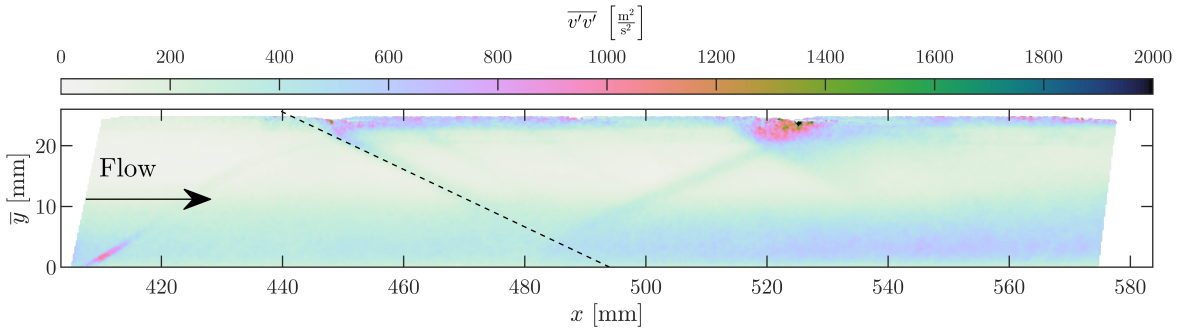
Fig. 19 Compilation of PIV mean velocity data for the $\alpha = 16°$, $\ell = 0$ interaction at $Re_D = 2 \times 10^6$.



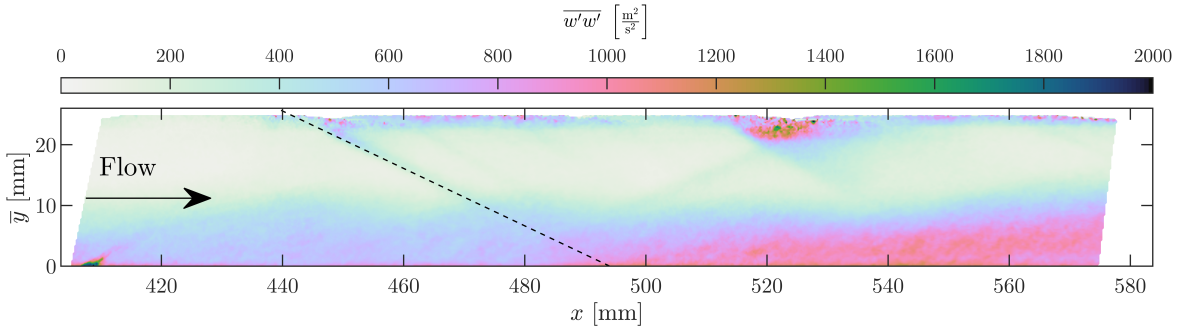
(a) Axial turbulence intensity, $\overline{u'u'}$.



(b) x-y plane shear stress, $\overline{u'v'}$.



(c) Wall-normal turbulence intensity, $\overline{v'v'}$.



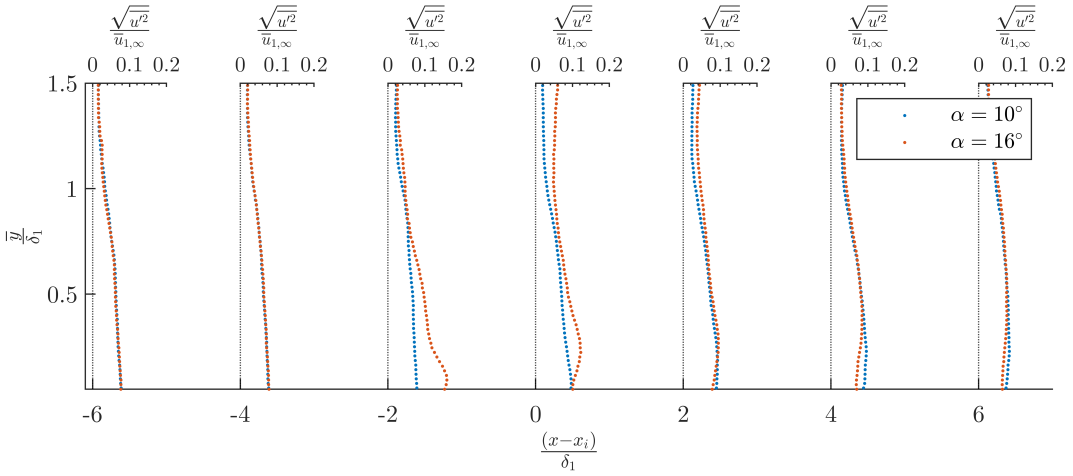
(d) Spanwise turbulence intensity, $\overline{w'w'}$.

Fig. 20 Compilation of PIV velocity fluctuation data for the $\alpha = 10°$, $\ell = 0$ interaction at $Re_D = 2 \times 10^6$.

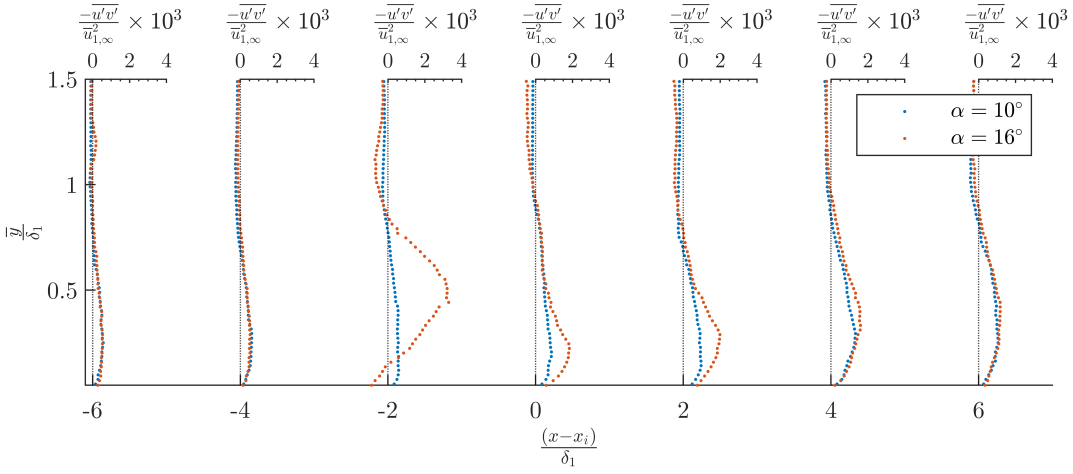
by the deceleration term, to peak at the mean location of the reflected shock foot. While $\overline{u'u'}$ is approximately 4–6 times larger than $-\overline{u'v'}$ at the shock foot, the wall-normal gradient of axial velocity peaks at a value about 3 times higher than the streamwise derivative. Thus, the complete dominance of the deceleration term is not simply explained by the relative peak magnitude of the component terms. The reason for the strong influence of the deceleration term becomes clear when analyzing the spatial correlation of the kinematic Reynolds stresses with their corresponding mean velocity gradient. For this analysis, data within the $-3 \leq \frac{x-x_i}{\delta_1} \leq -1.25$ and $0 \leq \frac{\overline{y}}{\delta_1} \leq 0.5$ region was extracted to isolate the region of primary streamwise turbulence generation. The bounds of this region are shown by the black box overlay in Fig. 22. The scattered data as well as contours of the joint probability density function and a best-fit linear correlation between the two quantities are shown in Figs. 23a and 23b. The standard R^2 coefficient was used as the metric to evaluate the level of correlation. As previously supposed, the streamwise normal turbulence is highly correlated with $\frac{\partial \overline{U}}{\partial x}$. The tightly grouped data on the lower left originates from the upstream undisturbed boundary layer. The data is grouped tightly around the best fit line for moderate levels of turbulence and then begins to become more scattered for the highest levels of local intensity. On the other hand, in-plane shear ($\overline{u'v'}$) shows very poor correlation with the wall-normal gradient in axial velocity over the selected region with the largest shear occurring in regions of near-zero local velocity gradient, which would yield no turbulence production. There are some distinct features visible in the scattered shear stress data, however. As with the streamwise turbulence, the source of the most concentrated data is the outer region of the upstream boundary layer, where there is a low gradient in the mean velocity and $\overline{u'v'}$ is near zero. There is a secondary cluster of data which arises from the reflected shock foot which shows the highest levels of turbulent shear stress in a location mean velocity gradient is only slightly elevated. There is an additional clustering of data at positive $\overline{u'v'}$ which coincides with the region of strongest $\frac{\partial \overline{U}}{\partial \overline{y}}$, which is also clearly visible in Fig. 19b. However, the overall correlation with mean velocity gradient is poor even when isolating this region.

The streamwise evolution of the distributions of turbulent fluctuations were also analyzed. At select distances from the wall, velocity data were compiled from the ensemble of instantaneous PIV measurement for the camera view which contained the primary interaction. A sampling of these distributions is shown in Fig. 24, where contours of probability are shown as a function of axial position and fluctuation strength. Here, not only the distribution width but also its skewness are observable. Well outside the boundary layer at $\frac{\overline{y}}{\delta_1} = 1.5$, the incoming flow shows a very narrow and symmetric u' distribution until the incident shock is met at approximately $\frac{x-x_i}{\delta_1} = -3$, which broadens the distribution slightly. This is followed by a narrowing of the distribution between the impinging and reflected shocks before the r.m.s. level rises again behind the reflected shock. At the boundary layer edge (Fig. 24b), the incoming flow has a distinct negative skewness, which was also observed in mass flux fluctuation distributions made by hot-wire measurements [7]. This is commonly attributed to the ejection events observed in turbulent boundary layers driven by hairpin vortices lifting into the wake region and delivering intermittent bursts of low-momentum fluid. The hot-wire technique, with its superior spatial/temporal resolution and number of samples in this experiment, is better suited for detailed study of these events and the associated flow structures. The skewness at the edge of the boundary layer appears to wane once the shock interaction is encountered with a concurrent moderate increase in turbulent intensity. This is due to the apparent fluctuations being dominated by reflected shock motion instead of vortical structures in the incoming turbulent layer. In the final example, the increase in streamwise turbulence intensity in the incoming boundary layer is clear. The mean reflected shock foot position is encountered at $\frac{x-x_i}{\delta_1} = -3$ in this profile, which coincides with a marked broadening of the distribution and a coincident bias toward negative fluctuations. At the furthest axial station, it appears that the distributions return to a symmetric behavior and the magnitude of fluctuations subsides as the region of highest turbulence is now passed (see Fig. 19a).

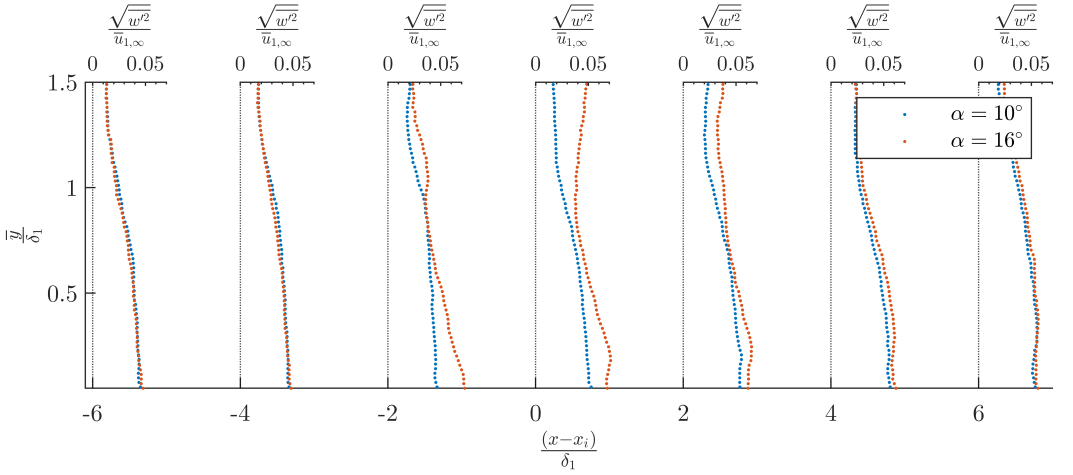
To further analyze the behavior of the turbulent fluctuation statistics, the standard deviation (equivalent to the r.m.s. fluctuation) and skewness of the distributions were computed and plotted as a function of streamwise position in Fig. 25. Far outside the initial boundary layer, the $\frac{\overline{y}}{\delta_1} = 1.5$ shows the lowest initial r.m.s. value and a skewness near zero (not identically zero due to the narrow distribution amplifying small deviations from symmetry, see Fig. 24a). The skewness, which is difficult to directly assess in Fig. 25, shows a distinct rise at the incident shock which remains constant until the reflected shock is met and the value returns to near zero. However, skewness values throughout this region are highly sensitive due to the relatively narrow distributions. Inspection of skewness data in the other 2 velocity components, which should exhibit symmetric distributions, show that the noise floor is approximately ±0.25 for this data. Similar behavior is observed at $\frac{\overline{y}}{\delta_1} = 1.25$, but with the distinctly negative incoming skewness providing a nearly constant reduction upstream of the reflected shock. The negative skewness in the incoming boundary layer turbulence is most pronounced at $\frac{\overline{y}}{\delta_1} = 1$. Here, the turbulence intensity is still only slightly elevated from the freestream value. At this height, the crossing of the impinging shock and the reflected shock foot are coincident. Proceeding deeper into the



(a) Axial turbulence intensity.



(b) In-plane shear stress.



(c) Spanwise turbulence intensity.

Fig. 21 Profiles of turbulent stresses at select stations through the $\alpha = 10°$ and $16°$ axisymmetric interactions, both at $Re_D = 2 \times 10^6$.

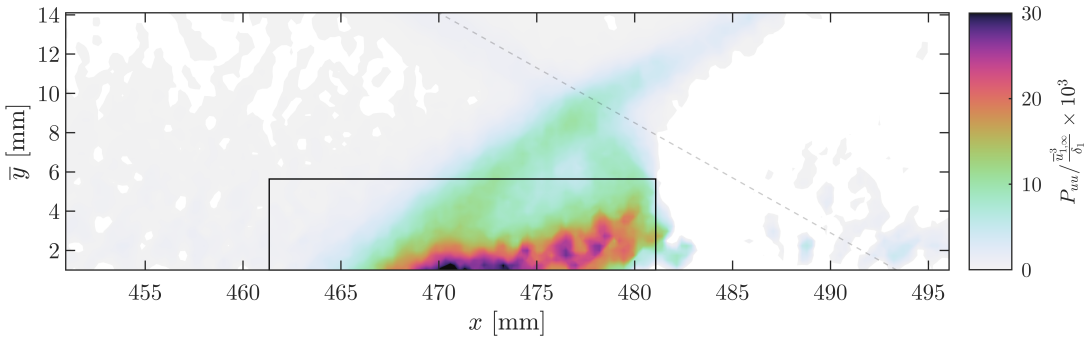
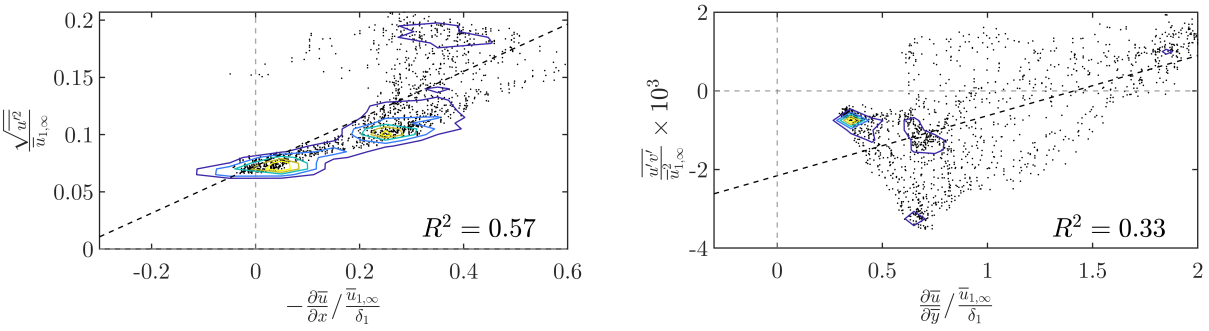
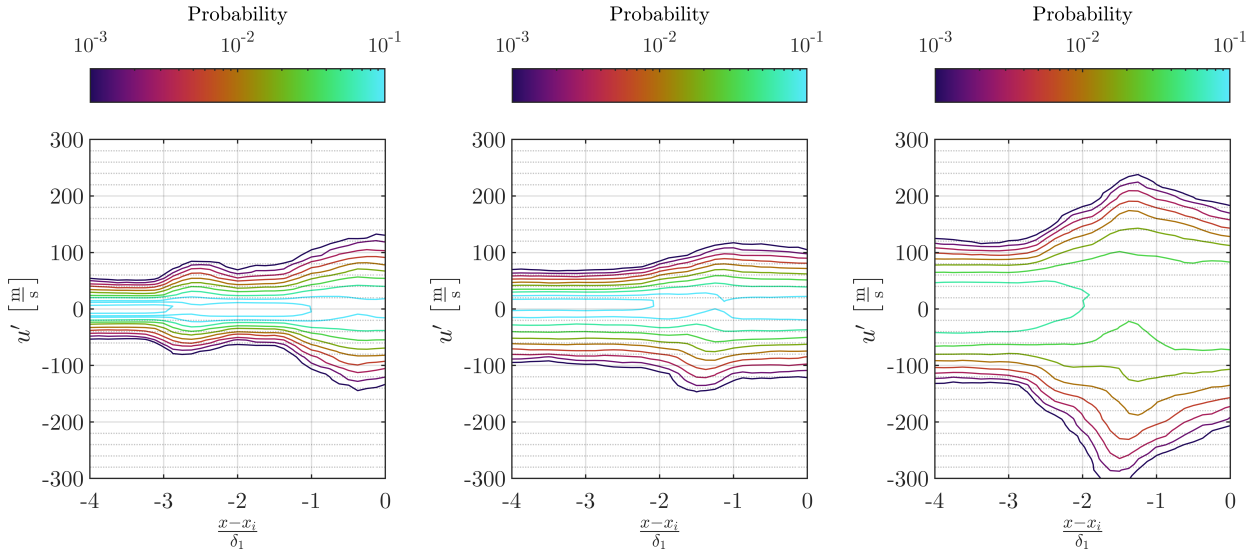


Fig. 22 Production of streamwise turbulence in the $\alpha = 16°$ interaction. *Black box shows interrogation region for scatter plots of Fig. 23.*



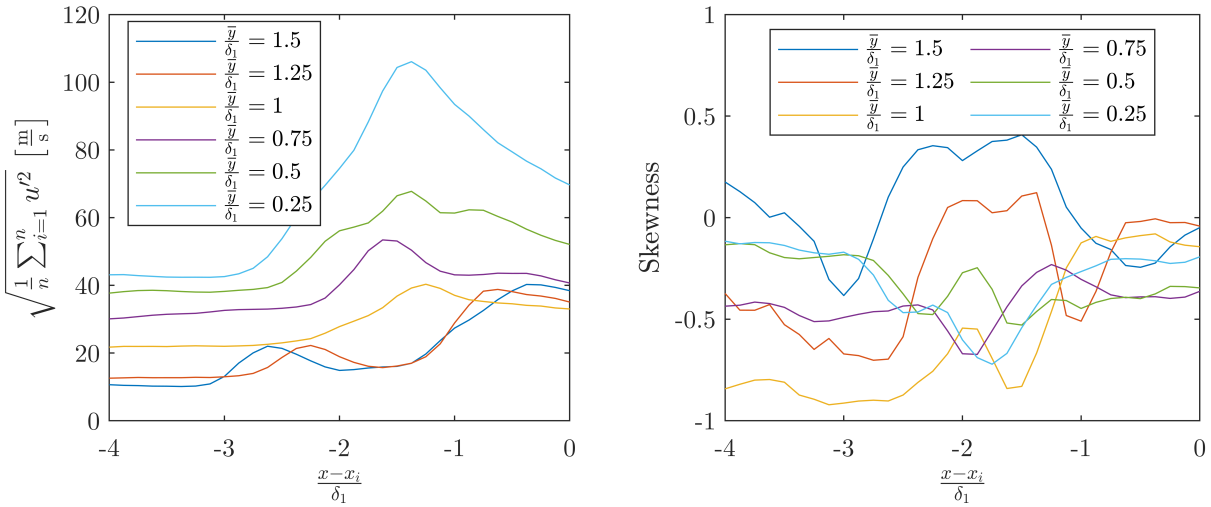
(a) $\overline{u'u'}$ **vs.** $\frac{\partial \overline{U}}{\partial x}$**.** **(b)** $\overline{u'v'}$ **vs.** $\frac{\partial \overline{U}}{\partial \overline{y}}$**.**

Fig. 23 Correlation of turbulence quantities with local mean velocity gradient within the region where $-3 \leq \frac{x-x_i}{\delta_1} \leq -1.25$ and $0 \leq \frac{\overline{y}}{\delta_1} \leq 0.5$.



(a) $\frac{\overline{y}}{\delta_1} = 1.5$**.** **(b)** $\frac{\overline{y}}{\delta_1} = 1.0$**.** **(c)** $\frac{\overline{y}}{\delta_1} = 0.25$**.**

Fig. 24 Axial velocity fluctuation (u') distributions as a function of x near the interaction region.



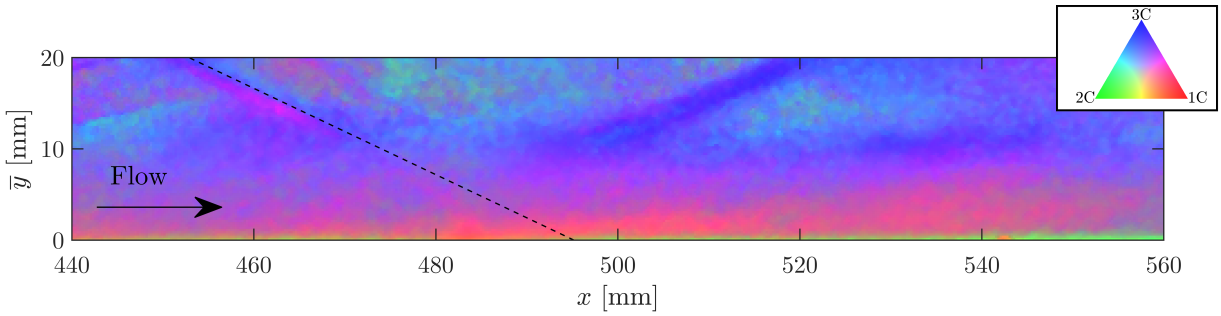
(a) Standard deviation. **(b) Skewness.**

Fig. 25 Axial velocity fluctuation (u') distribution metrics as a function of x near the interaction region.

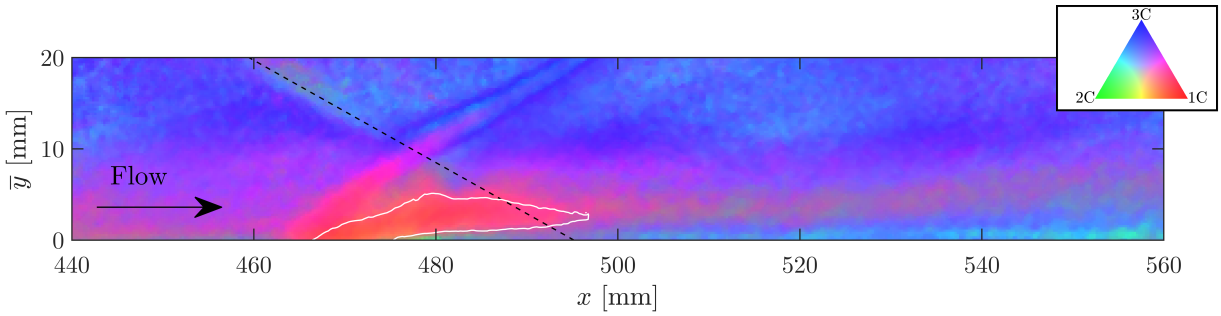
boundary layer, the profiles show the same general character, where the distribution widths begin to rise where the reflected shock foot is encountered, reach a peak value, and then decay back toward the freestream value. The skewness for each of these heights is fairly noisy with the only significant feature being the negative dip in the $\frac{\overline{y}}{\delta_1} = 0.25$ profile Interestingly, the streamwise turbulence appears to approach a symmetric distribution downstream of the interaction at all wall-normal distances. However, this behavior does not persist further downstream of the interaction. By performing the same analysis on the downstream camera positions, it was confirmed that the boundary layer begins to show the same behavior as the incoming undisturbed profile. At $\frac{x-x_i}{\delta_1} = 3$ the negative skew has reestablished in the outer portion of the layer with a value of approximately -1 at $\frac{\overline{y}}{\delta_1} = 1$ as the layer begins to return to equilibrium. The turbulence strength, as seen in Fig. 21a, remains elevated within the boundary layer relative to the undisturbed incoming flow at the furthest downstream location of $\frac{\overline{y}}{\delta_1} = 7$. Data for camera views are not shown due to their unremarkable behavior. While continuous profiles of various turbulence distribution moments through the entire PIV sampling range are obviously desirable, they are not presented here due to the ambiguity of combining fluctuation data within the overlap region between camera views.

The turbulence behavior through these interactions can be further analyzed through inspection of the anisotropy. Because all 3 components of velocity are measurable by the PIV technique, the full Reynolds stress tensor can be computed at each spatial location. The behavior of this tensor is typically characterized by mapping the invariants on a 2D plot such as a "Lumley triangle" [37], turbulence triangle [38], or a barycentric map [39] to identify the turbulence state. However, this technique is not readily applicable to spatial fields of data; thus, the visualization technique proposed in Ref. 40 was adopted where the tensor state within the barycentric coordinates are mapped to a colormap which visually denotes the proximity to each of the 3 limiting states. This method was applied to the stresses obtained by PIV measurement and is presented in Fig. 26. In the current implementation, the color blue was used to represent the isotropic state (spherical Reynolds stress ellipsoid, denoted as "3C"), green for the two-component axisymmetric state (disk-shaped Reynolds stress ellipsoid, denoted as "2C"), and red for the single-component limiting case (Reynolds stress ellipsoid collapses to a line, labeled "1C" in the figure). In the flow upstream of the interaction, the expected wall-bounded turbulence behavior is obtained where the isotropic freestream moves toward one-component behavior along the right-hand boundary of the Lumley triangle as the distance from the wall decreases. Very near the wall, the turbulence should become two-component in nature as the v' is suppressed by proximity to the wall. As previously noted, the $\alpha = 10°$ interaction has only a minor effect on the boundary layer behavior, primarily by thickening it. For the $\alpha = 16°$ configuration, a strong shift toward strong "cigar-shaped" behavior (pink) along the reflected shock foot which transitions toward the 1-D state as u' becomes the dominant component. This is illustrated in Fig. 26b by the collocation of the red coloring with the region of highest turbulent kinetic energy (TKE). This continues within the interaction region where streamwise normal stress remains elevated up to the inviscid impingement line (see Fig. 19a). Beyond the

interaction, the turbulence has clearly not returned to typical boundary layer behavior at the downstream bound of the region sampled by PIV. The anisotropy field roughly aligns with the behavior observed in LES of a planar impinging wave interaction [41] where the shortcomings of standard RANS turbulence closures are also illustrated.



(a) $\alpha = 10°$**.**



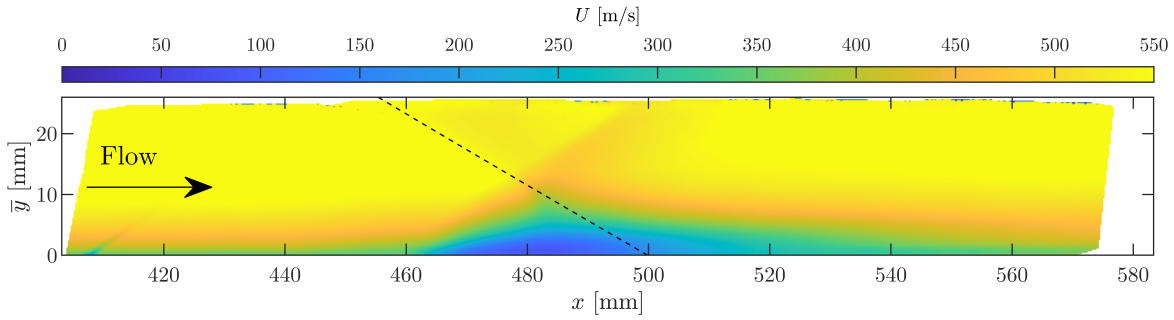
(b) $\alpha = 16°$**.**

Fig. 26 Barycentric anisotropy mapping for axisymmetric interactions at $Re_D = 2 \times 10^6$**.** *White line indicates the region where the TKE exceeds* $6u_{\tau 1}^2$.

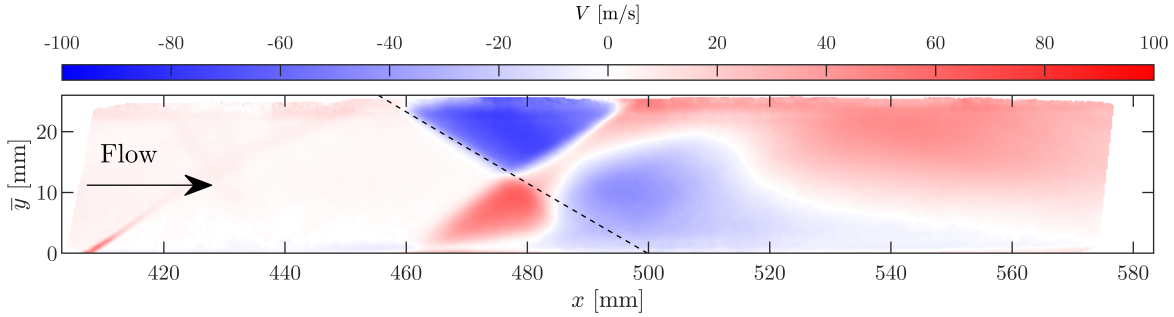
C. Swept Interactions

By shifting the shock generator away from the test section axis, a variety of swept shock configurations can be generated in the region accessible by PIV measurement. As previously discussed in Section II.B, only the $\ell = \frac{R}{4}$ offset was used in this test entry. PIV data was of particular interest for the $\overline{\theta} = 90/270°$ position due to the difficulty in making a probe measurement in that interaction [7]. In this highly swept interaction, the flow direction turns rapidly near the wall, requiring specialized probe geometry tailored specifically for this application. However, because a stereoscopic PIV measurement was made, all three velocity components of the flow can be quantified in this region. The three velocity component mean fields for the $\alpha = 16°$ shock generator in this configuration are shown in Fig. 27. The $\overline{u}$ and $\overline{v}$ fields appear qualitatively to be very similar to the axisymmetric case, with the primary departure being an increase in upstream influence in the swept interaction. Figure 27c shows the magnitude of spanwise velocity which occurs near the wall in this case. Regions of extreme flow yaw near $\overline{\theta} = 90°$ have been previously observed in swept interactions [42]. Here, the peak $\overline{w}$ value is approximately 20% of the freestream $\overline{u}$ value, which agrees well with the simulations of similar geometry at reduced Reynolds number in Ref. 35. The region of $|\overline{w}| > 100$ m/s extends for approximately $3\delta_1$ in the axial direction and up to $0.3\delta_1$ from the wall. It is also noteworthy that the region of high gradient in the spanwise velocity is not coincident with the high gradient region in axial velocity. This occurs nearer to the wall in the spanwise component, which will be investigated further in subsequent figures.

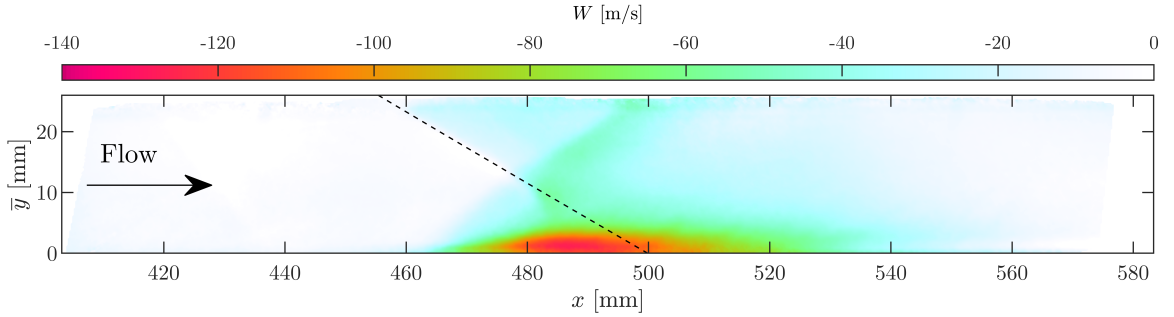
Figure 28 shows a more detailed picture of the boundary layer mean velocity through the interaction. Velocity profiles are extracted at select stations and plotted against the corresponding quantity from the axisymmetric configuration (Fig. 18). The swept interaction shows a stronger deficit in axial velocity (Fig. 28a) which occurs prior to the location of maximum velocity defect in the axisymmetric case. This increase in upstream influence for the swept interaction is consistent with the static pressure and oil flow visualization results in Ref. 8. The outer region of these profiles show



(a) Axial velocity, U.



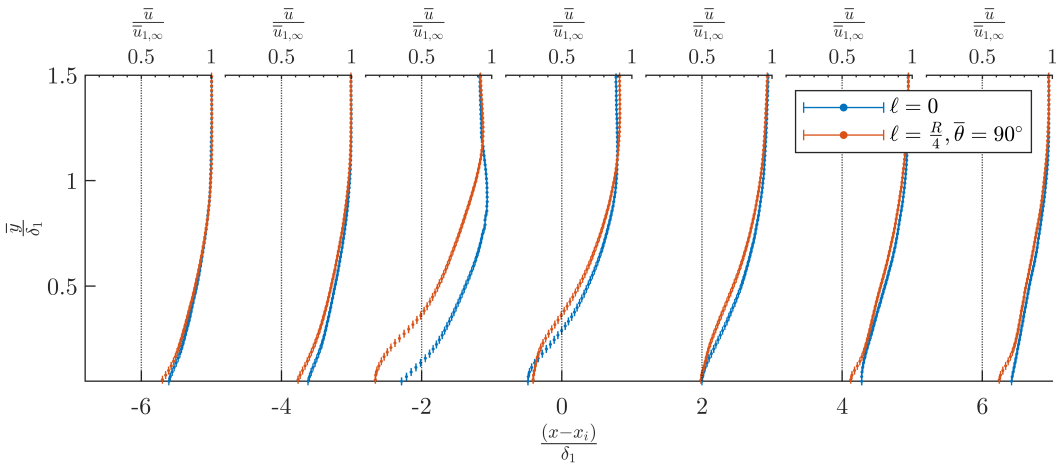
(b) Wall-normal velocity, V.



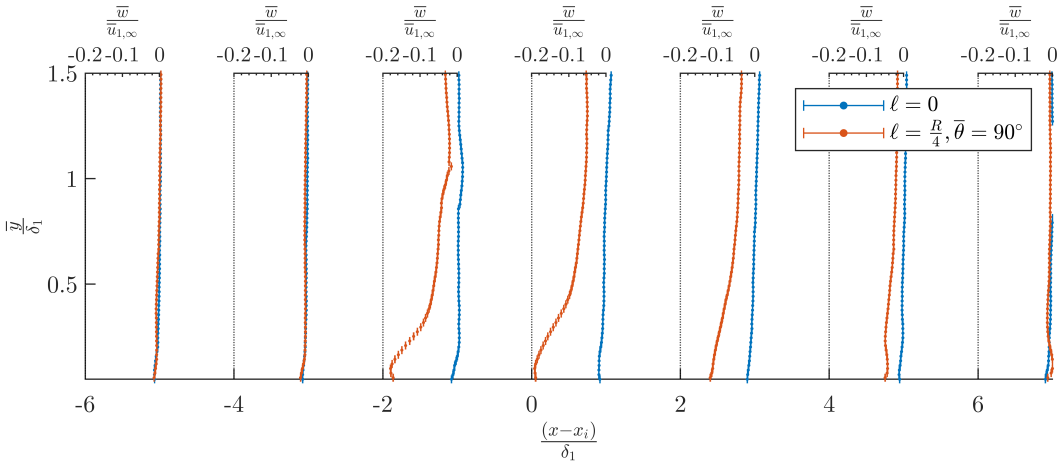
(c) Spanwise velocity, W.

Fig. 27 Compilation of PIV mean velocity data for the $\alpha = 16°$, $\ell = \frac{R}{4}$, $\overline{\theta} = 90°$ interaction at $Re_D = 2 \times 10^6$.

nearly identical behavior and the two cases are observed to converge to a similar behavior by the furthest downstream station presented. The spanwise velocities shown in Fig. 28b highlight the strong out-of-plane velocity component present in the swept interaction. In the normalized units used here, it is clearly shown that the W component reaches 20% of the freestream axial velocity in the near-wall region while the freestream magnitude is only 4% of $\bar{u}_{1,\infty}$.



(a) Axial velocity, U.



(b) Spanwise velocity, W.

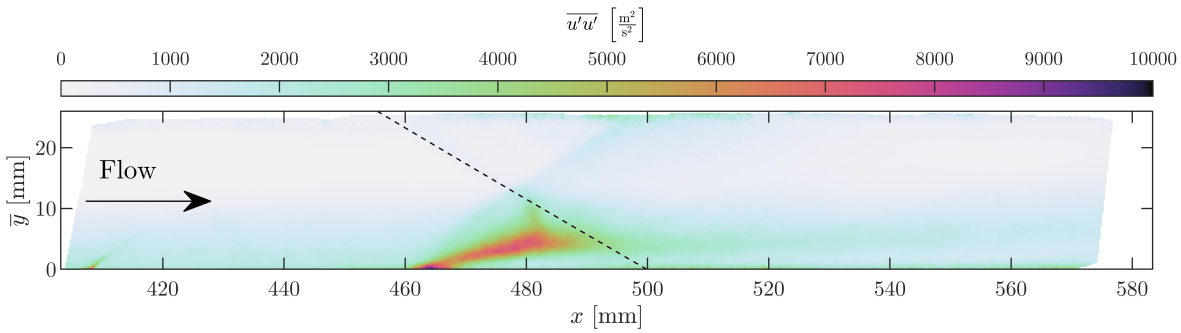
Fig. 28 Profiles of mean velocity at select stations through the $\alpha = 16°$, $\ell = \frac{R}{4}, \overline{\theta} = 90°$ interaction in comparison with the axisymmetric baseline, both at $Re_D = 2 \times 10^6$. *Dashed lines indicate the sampling station (lower abscissa). Error bars indicate 3 times the local standard error of the mean.*

The velocity fluctuation fields for the swept interaction are presented in Figs. 29 and 30. In both figures, the color scale limits were maintained at the values from Fig. 19 for ease of comparison. In general, each shows a qualitatively similar behavior to its axisymmetric counterpart with some subtle alterations.

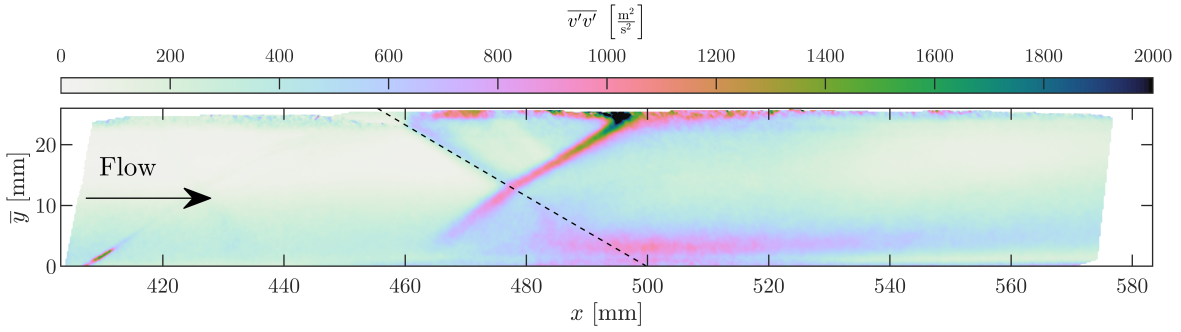
The 3 normal turbulence intensities are presented in Fig. 29. The axial component shows a similar behavior to the axisymmetric separated interaction (Fig. 19a) with a region of strong turbulence which emanates from the reflected shock foot and moves away from the wall with downstream distance. In the swept interaction, the magnitude of the quantity is somewhat reduced, likely due to relief in the spanwise direction. Similarly, turbulence in the wall-normal direction appears very similar to the axisymmetric case where most of the energy is near the reflected shock with an additional broad enhancement within the boundary layer just downstream of the interaction. Spanwise turbulence, most interestingly, appears quite similar to the unswept interaction. The general similarity of the qualitative behavior of the turbulence to that of the axisymmetric interaction indicates that the strong three-dimensionality in the mean has only a

minor effect on the normal components of the Reynolds stress tensor.

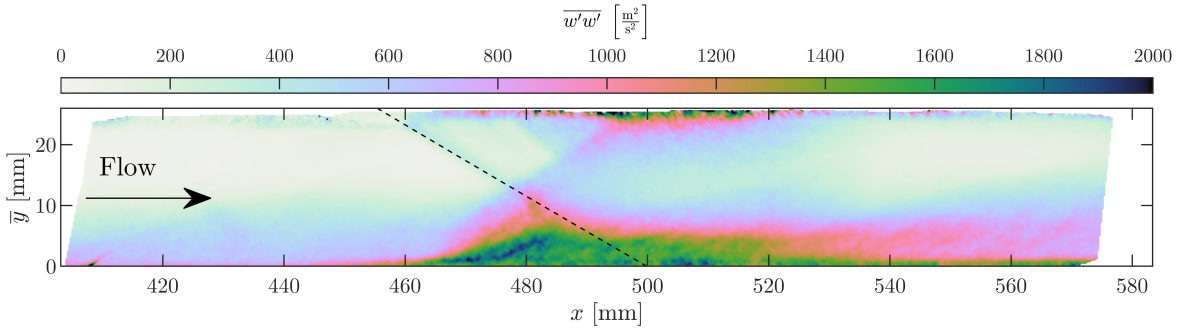
All 3 shear components of turbulent stress are also presented in Fig. 30. Additional components are shown that were insignificant in Section III.B due to the spanwise flow present in the swept interaction. For reference, the values of $\overline{u'w'}$ and $\overline{v'w'}$ in the axisymmetric interaction are both less than 2% of freestream velocity over 95% of the region surveyed, respectively. As with the axisymmetric interaction at the same α, the in-plane shear stress is dominated by artificially elevated magnitude caused by reflected shock motion. The swept interaction does show the region of large negative $\overline{u'v'}$ to be more broadly distributed aft of the line of peak strength. The small region of reversed shear observed in the axisymmetric interaction is also less concentrated in the swept interaction and, thus, does not exhibit as pronounced of a peak region. The $\overline{u'w'}$ field shows a strong negative value in the vicinity of the shock crossing and along a line which roughly traces the region of high $\frac{\partial W}{\partial y}$. This spatial correlation will be analyzed in detail. The presence of significant turbulent shear in this plane is the distinguishing feature of the turbulent behavior of this interaction relative to the axisymmetric case. The strongest shear in the y-z plane, on the other hand, appears in the reflected shock outside of the boundary layer. This is a region of significant spanwise velocity (up to 10% of $\bar{u}_{1,\infty}$).



(a) Axial turbulence intensity, $\overline{u'u'}$.

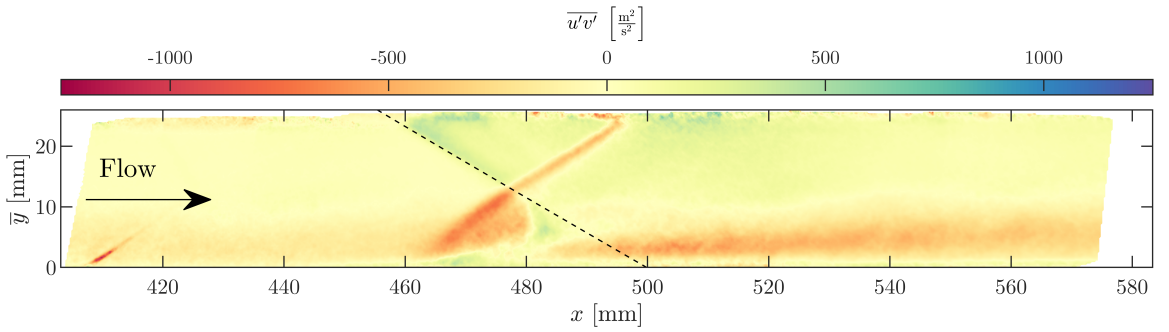


(b) Wall-normal turbulence intensity, $\overline{v'v'}$.

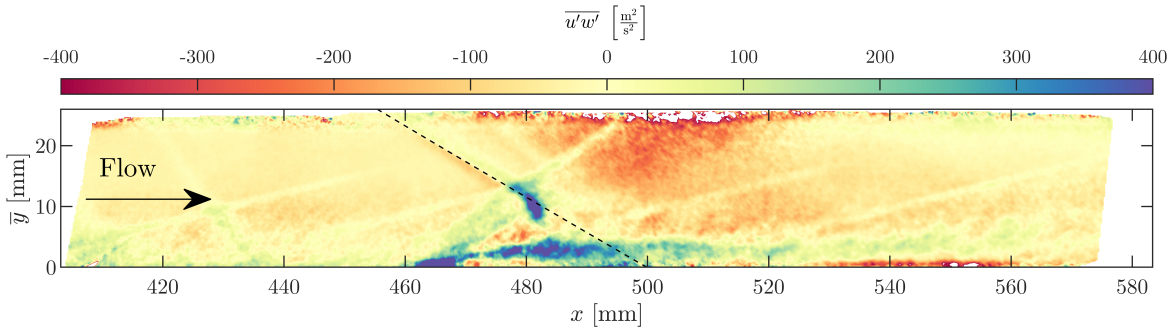


(c) Spanwise turbulence intensity, $\overline{w'w'}$.

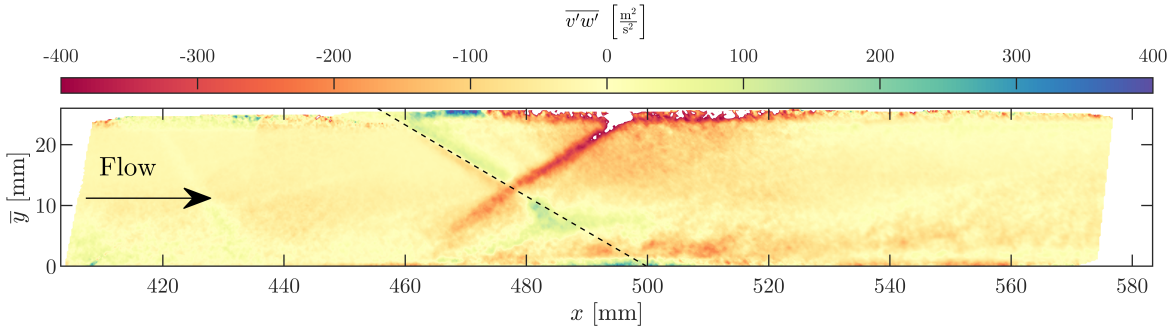
Fig. 29 Compilation of PIV turbulence intensity data for the $\alpha = 16°$, $\ell = \frac{R}{4}$, $\overline{\theta} = 90°$ interaction at $Re_D = 2 \times 10^6$.



(a) x-y plane shear stress, $\overline{u'v'}$.



(b) x-z plane shear stress, $\overline{u'w'}$.



(c) y-z plane shear stress, $\overline{v'w'}$.

Fig. 30 Compilation of PIV Reynolds shear stress data for the $\alpha = 16°$, $\ell = \frac{R}{4}$, $\overline{\theta} = 90°$ interaction at $Re_D = 2 \times 10^6$.

Figure 31 provides a direct comparison of the turbulence quantities from the swept interaction against the corresponding axisymmetric values at select stations. The axial turbulence profiles highlight the larger upstream influence of the swept interaction. At $2\delta_1$ upstream of the inviscid impingement point, the peak turbulence level is nearly identical at 14–15% of $\bar{u}_{1,\infty}$ but occurs further from the wall in the swept interaction. With the necessarily sparse spacing used in the figure, the location of peak turbulence in the axisymmetric case is not shown. However, evidence of the higher levels in the axisymmetric case are present in the subsequent profiles as those profiles show a distinctly higher peak than in the swept version. By the final station, the two profiles are nearly identical save for a near-wall anomaly which is driven by low vector yield in that region. As seen in Fig. 29c, the spanwise turbulence intensity is very similar between the two interactions. In fact, the only appreciable difference any profile is at $\frac{x-x_i}{\delta_1} = 2$ where the swept interaction shows as slightly elevated turbulence level. Each interaction shows an initial enhancement above the reflected shock foot of up to 5% of $\bar{u}_{1,\infty}$ which shifts outward from the wall with downstream distance. The furthest downstream station shows a nearly flat profile within the boundary layer. The x-y plane shear stress shows the largest discrepancy between the two interactions (beyond the obvious out-of-plane enhancements). Here, the swept interaction

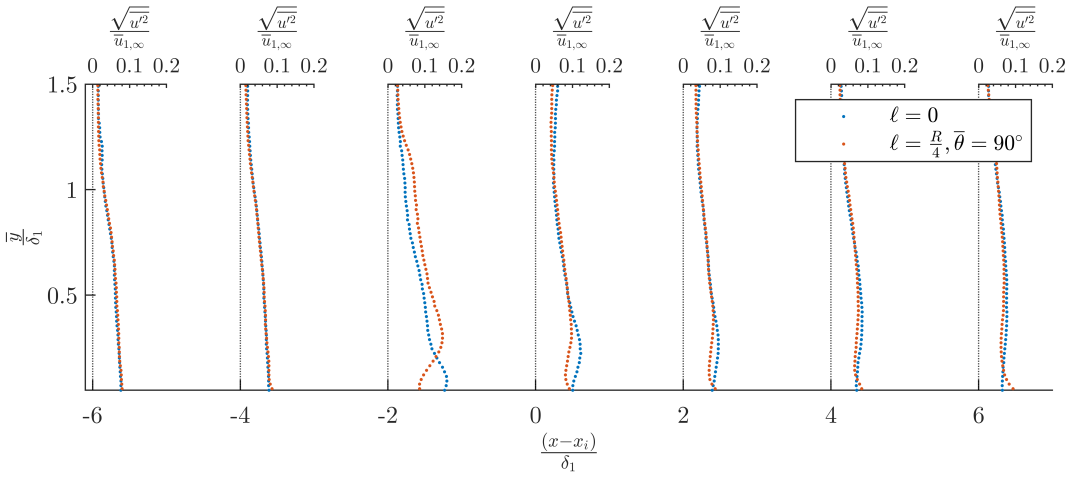
shows a reduced level of peak shear in the reflected shock foot. The shear in this region also appears, in the mean, to be distributed over a larger wall-normal region. This is likely due to larger excursions of the reflected shock foot from its mean position, which would require a more further measurements and analysis. The post-interaction behavior of this quantity is similar among the two interactions with a slow diffusion with downstream distance.

Because of the three-dimensionality of the flow and the lack of gradient information in the z direction, the turbulence production cannot be directly evaluated for this interaction. However, the spatial correlation of kinematic Reynolds stresses with mean velocity gradient within the interaction region may be analyzed as in Fig. 23 with the acknowledgment that the total production is not being quantified. Figure 32 shows the scattered data as well as contours of the joint probability density function and a best-fit linear correlation between quantities which are multiplied to form terms in the axial and spanwise turbulence components. The standard R^2 coefficient is again presented on each figure for the best-fit linear regression. As in the axisymmetric interaction, streamwise turbulence production is dominated by the deceleration term ($\overline{u'u'}\frac{\partial \overline{u}}{\partial x}$). The scatter plots for streamwise turbulence production quantities in this interaction appear qualitatively similar to the Figs. 23a and 23b with the primary difference being the reduction in peak $\overline{u'u'}$ and $\overline{u'v'}$. Again, the strongest shear occurs in regions of minimal $\frac{\partial \overline{u}}{\partial \overline{y}}$ and, thus, the shear-induced production is dwarfed by the deceleration term. The production of spanwise turbulence in the selected region is influenced more by shear in the x-z plane rather than y-z. This is shown in Figs. 32c and 32d where the low magnitude of the $\overline{v'w'}$ shear renders that term negligible. Because the region of high $\overline{w}$ resides further downstream of the reflected shock foot (compare Figs. 27a and 27c), the high $\frac{\partial \overline{w}}{\partial \overline{y}}$ magnitude and non-zero levels of $\overline{v'w'}$ combine to reverse this behavior near the inviscid impingement point. This is shown in Fig. 33. Here, the near-zero levels of $\frac{\partial \overline{w}}{\partial x}$ negate the $\overline{u'w'}$ shear as well. It is important to note that the spanwise gradient term, $\frac{\partial \overline{w}}{\partial z}$, which is not quantified in the current dataset, is likely to be the dominant producer of spanwise turbulence in both interrogation regions.

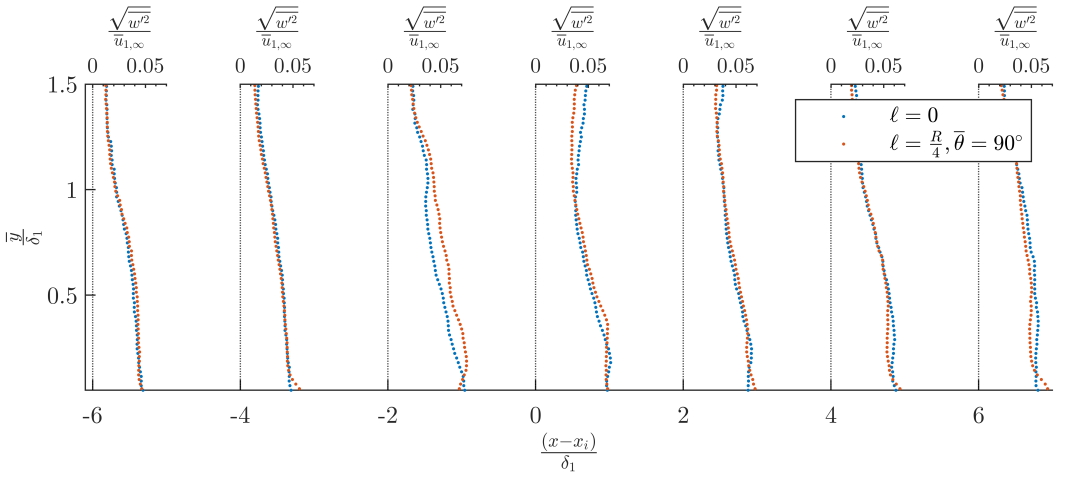
In Fig. 34, axial profiles of the standard deviation and skewness of the streamwise turbulence are shown at select heights from the test section wall as in in Fig. 25. The profiles from the axisymmetric interaction are also shown as dotted lines for reference. The first thing to note is the relatively similar appearance of the profiles overall in both plots. Working from the freestream to the wall, it is clear that the hyperbolic shock trace projected in the measurement plane is shallower than the conical version, as the first influence on the $\frac{\overline{y}}{\delta_1} = 1.5$ profile occurs upstream in the swept interaction. The two interactions show a very similar peak level at both the incident and reflected shocks with a similar plateau between. As we move into the boundary layer, the profiles from the two interactions appear to behave nearly identically up until the $\frac{\overline{y}}{\delta_1} = 0.25$ where the streamwise turbulent intensity continues to a much higher peak in the axisymmetric interaction. This is apparent under close inspection of Fig. 19a and Fig. 29a, but was not captured by the sparse axial spacing of the profiles in Fig. 31a. In the skewness profiles, the behavior upstream of the interaction is roughly identical, as it should be, and the level of mismatch aligns with the uncertainty in this quantity. For example, the increase in the skewness magnitude at the $\frac{\overline{y}}{\delta_1} = 1$ height is almost certainly not reflective of an change in the local intermittency of the incoming boundary layer, but instead due to the sensitivity of the skewness metric to noise for a relatively narrow distribution. Downstream of the incident shock, the profiles further from the wall are noticeably lacking the increase in skewness observed in the axisymmetric case. However, as described previously, the skewness value is likely influenced by the narrowness of the distribution in this region. As in the axisymmetric case, all distributions appear to coalesce toward symmetry at the aft end of this camera view. The negative skewness expected at the edge of the boundary layer does return in this interaction as well, but not until the $\frac{x-x_i}{\delta_1} > 4.5$.

Due to the mean out-of-plane velocity inherent to the swept interaction, the distributions of w' were also analyzed using the methods applied to the axial velocity data. The standard deviation and skewness as a function of axial position are presented in Fig. 35 for the same select wall-normal heights. As in the axial component, the turbulent intensity levels in the out-of-plane velocity are nearly identical between the swept and symmetric interactions (seen previously in wall-normal profiles of Fig. 31b). The only noticeable difference is the forward advance of the initial interaction with the shock for $\frac{\overline{y}}{\delta_1} \geq 0.75$ due to the difference in projected shock angle. The magnitude of the intermediate peaks in spanwise turbulence appear quite similar except for the slightly enhanced magnitude at the furthest downstream extent of this camera view. This difference subsides in subsequent camera views (not shown). The skewness profiles shown in Fig. 35b illustrate that the w' distributions are nearly symmetric across the interaction, with the only significant deviation occurring outside of the boundary layer at the station where the profile crosses the reflected shock. This is likely a shock motion artifact rather than a feature of the turbulence behavior.

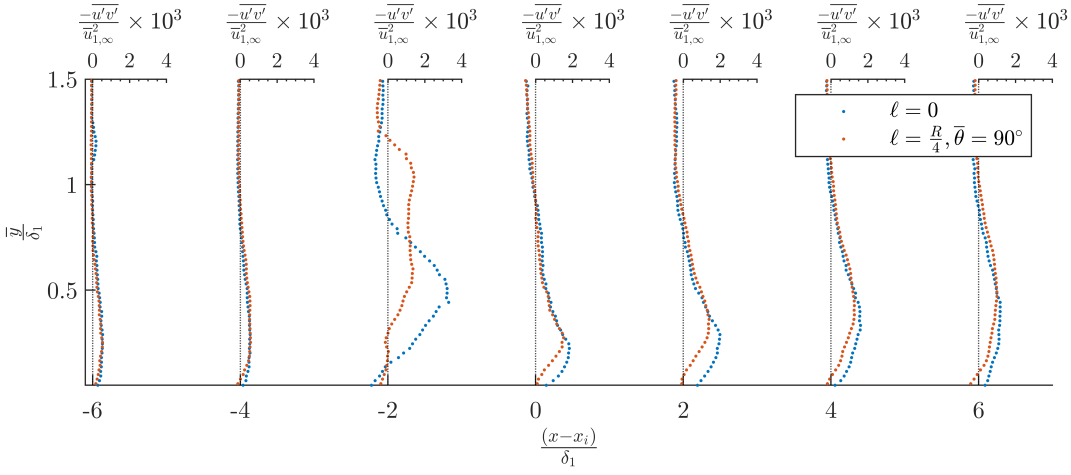
As in the axisymmetric interactions, the turbulence anisotropy was also investigated for the swept interaction of primary interest at $\alpha = 16°$. Figure 36 presents the anisotropy tensor invariants for this flow mapped onto the barycentric coordinate system previously defined. Through the reflected shock foot, this interaction appears to mimic



(a) Axial turbulence intensity.

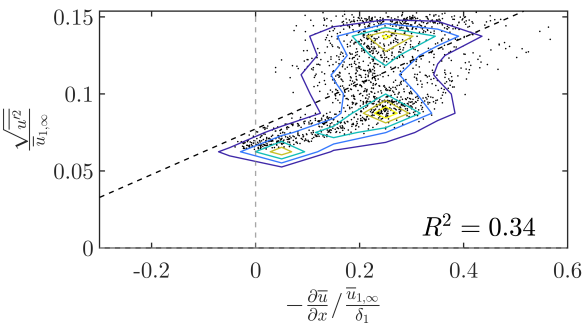


(b) Spanwise turbulence intensity.

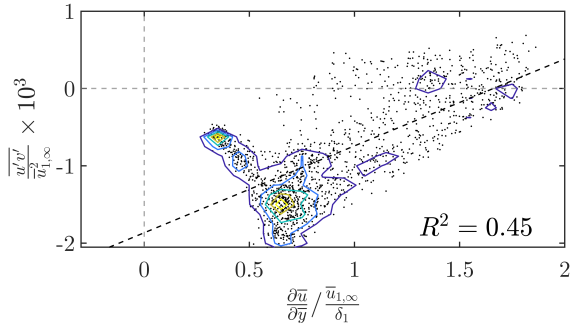


(c) In-plane shear stress.

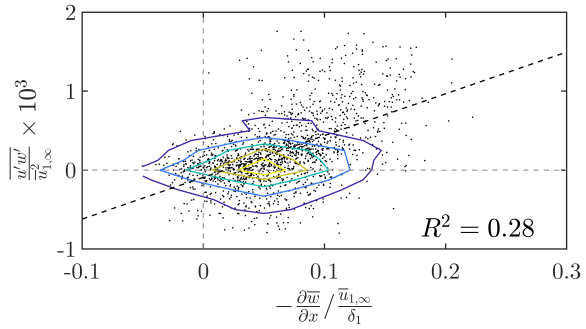
Fig. 31 Profiles of turbulent stresses at select stations through the $\alpha = 16°$, $\ell = \frac{R}{4}$, $\overline{\theta} = 90°$ interaction in comparison with the axisymmetric baseline, both at $Re_D = 2 \times 10^6$.



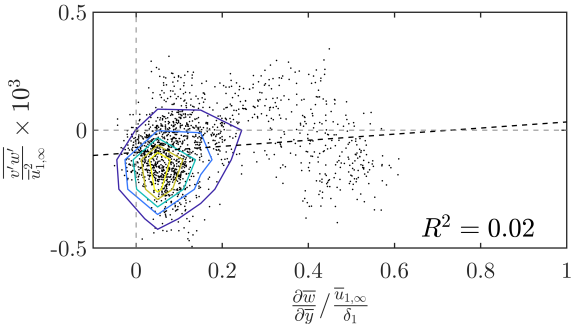
(a) $\overline{u'u'}$ **vs.** $\frac{\partial \overline{U}}{\partial x}$**.**



(b) $\overline{u'v'}$ **vs.** $\frac{\partial \overline{U}}{\partial y}$**.**

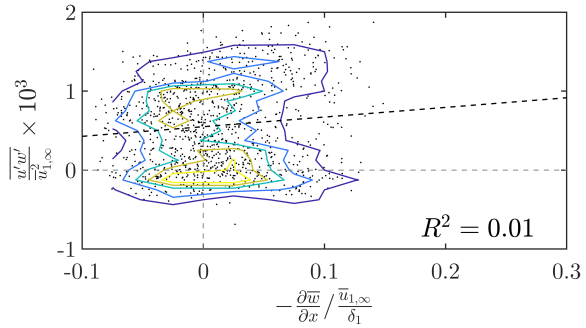


(c) $\overline{u'w'}$ **vs.** $\frac{\partial \overline{W}}{\partial x}$**.**

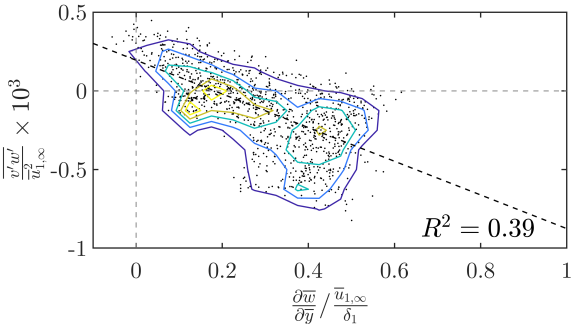


(d) $\overline{v'w'}$ **vs.** $\frac{\partial \overline{W}}{\partial y}$**.**

Fig. 32 Correlation of turbulence quantities with local mean velocity gradient within the region where $-3 \leq \frac{x-x_i}{\delta_1} \leq -1.25$ **and** $0 \leq \frac{\overline{y}}{\delta_1} \leq 0.5$**.**

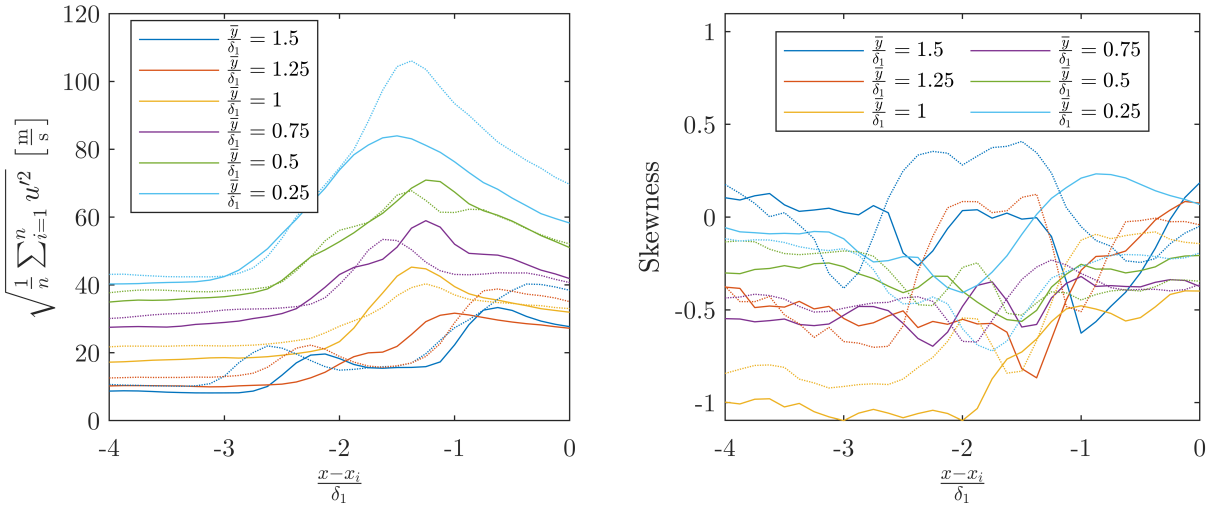


(a) $\overline{u'w'}$ **vs.** $\frac{\partial \overline{W}}{\partial x}$**.**



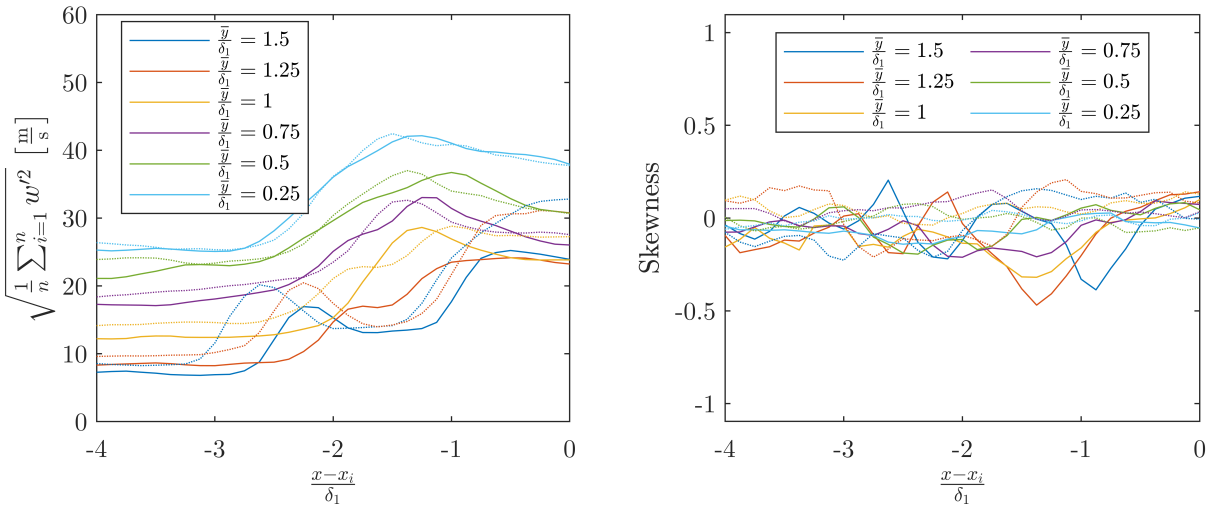
(b) $\overline{v'w'}$ **vs.** $\frac{\partial \overline{W}}{\partial y}$**.**

Fig. 33 Correlation of turbulence quantities with local mean velocity gradient within the region where $-1.25 \leq \frac{x-x_i}{\delta_1} \leq 0$ **and** $0 \leq \frac{\overline{y}}{\delta_1} \leq 0.5$**.**



(a) Standard deviation. **(b) Skewness.**

Fig. 34 Axial velocity (u') fluctuation distribution metrics as a function of x near the interaction region. *Dashed lines indicate the values from the symmetric interaction.*



(a) Standard deviation. **(b) Skewness.**

Fig. 35 Spanwise velocity fluctuation (w') distribution metrics as a function of x near the interaction region. *Dashed lines indicate the values from the symmetric interaction.*

the axisymmetric case at the same α with the initial jump to 2 Here also the region of single-component turbulence aligns closely with the region of highest TKE. In this flowfield, this occurs at an increased distance from the wall. Beneath this region, a pocket of nearly axisymmetric 2-component behavior forms, which becomes more isotropic as the region of high $\overline{w}$ is encountered. Post-interaction, the turbulence in the outer region of the boundary layer behaves more isotropically than is expected for a wall-bounded flow, as was observed in the axisymmetric interaction. Near the wall, strong axisymmetric two-dimensional behavior reappears which persists through the downstream boundary of the region surveyed by PIV.

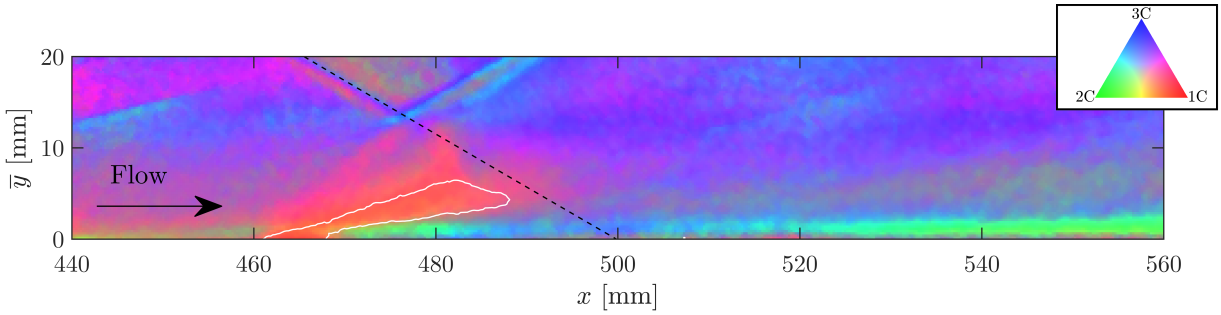


Fig. 36 Barycentric anisotropy mapping for the $\alpha = 16°$, $\ell = \frac{R}{4}$, $\overline{\theta} = 90°$ interaction at $Re_D = 2 \times 10^6$. *White line indicates the region where TKE is greater than $6u_{\tau 1}^2$.*

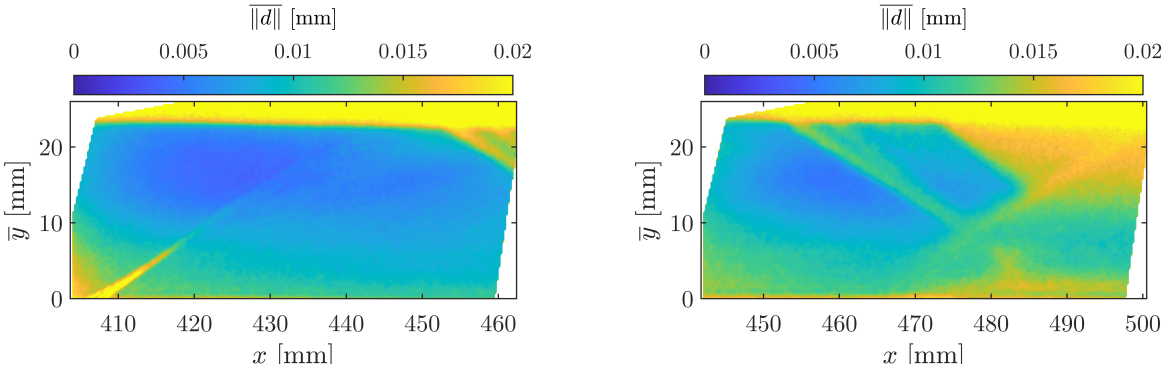
D. PIV Measurement Uncertainty

The velocity uncertainty of the PIV cross-correlation process is estimated by DaVis based on statistics of the observed correlation peak [43]. This method captures many common errors associated with practical PIV measurement in complex flowfields (seeding density, velocity gradients, out-of-plane motion). The 95% confidence bound for the uncertainty in mean velocity magnitude does not exceed 2% of $\overline{u}_{1,\infty}$ for all the cases shown, typically peaking near the reflected shock foot and falling to 0.1% in the incoming freestream. A possible future avenue for further assessment of the particle displacement error is the collection of PIV images at several pulse separation times to disentangle the random error from the turbulence within the underlying flowfield [44]. As discussed in Section III.A, applying this type of trade study across all test conditions is infeasible and a reduced scope of interactions would need to be selected for detailed analysis.

Calibration error was minimized in this experiment by using a stereoscopic self-calibration procedure [45] in addition to the initial target-based approach. This method makes small adjustments in laser plane location by cross-correlating the two camera views of the same laser pulse and minimizing the disparity. However, the ability of the polynomial camera calibration equations to completely account for the distortions of the convoluted optical path is strained in this application. The ultimate error in PIV measurement associated with the camera calibration can be quantified by the stereoscopic velocity reconstruction error. This is shown for two most upstream camera views in Fig. 37. The error in the upstream view is relatively benign, ranging from 0.25 pix in the freestream to 0.5 pix at the wall. The region of highest reconstruction error occurs at the shock waves, reaching 1 pix. As mentioned, motion of the shock wave dominates the turbulent statistics in this region; thus, the reconstruction error is not the primary concern. Precisely how this error propagates to the ultimate velocity measurements is an open question, but is estimated to be $< 5\%$ of $\overline{u}_{1,\infty}$.

The accuracy and precision of the electronics used to control the timing of the various PIV equipment has a strong effect on the measurement uncertainty. Due to the relatively short time delay required by the high freestream velocity and small spatial scale of the current experiment, the timing precision becomes even more crucial. For The PIV system used herein, the manufacturer specified output jitter for the pulse generator (LaVision PTU X) is 50 ps. In practice, this uncertainty is dwarfed by jitter in the delay between Q-switch trigger and actual laser output which ultimately drives the variability in time delay between the two laser pulses. This uncertainty was quantified with a photodiode and oscilloscope with high sampling rate, resulting in a $< 0.5\%$ (2.5 ns) timing error with 95% confidence.

Some influence of finite seed particle is inherent to any particle-based velocity measurement technique when applied in a turbulent flow. This results in a low-pass filtering effect in velocity data which is minimized by reducing the seed particle size or material density. With a quadratic dependence of Mie scattering cross section on particle scale, a balance



(a) View 1 (upstream of interaction). **(b) View 2 (containing interaction).**

Fig. 37 Average stereo reconstruction error magnitude for camera views of primary interest in axisymmetric $\alpha = 16°$ interaction at $Re_D = 2 \times 10^6$.

must be struck between providing adequate scattered light and faithful tracking of the full range of possible turbulent accelerations. In the current work, the seeding system was operated to provide the minimum seed particle size available. As discussed in Section III.A, the effects of seed particle inertia is noticeable in the boundary layer turbulent fluctuation magnitudes. This is attributed to a local influence of non-continuum effects which continually depresses the particle drag closer to the wall. The situation is further complicated by the polydispersity of the particle size distribution, which can yield varying levels of particle tracking error even within each interrogation window. Thus, a precise quantification of the uncertainty in the turbulence quantities due to particle inertia is beyond the scope of this work.

IV. Conclusions

A new stereoscopic particle image velocimetry (PIV) measurement capability has been applied to make detailed measurements in an impinging shock-wave/boundary-layer interaction (SWBLI) flowfield in a test section of circular cross-section. By virtue of this test section geometry, the flowfields studied are free from effects of the complex coupling of sidewall and corner interaction into the primary impinging shock interaction. Data was collected for both axisymmetric and swept interactions of varying impinging shock strength and over a range of Reynolds numbers. The focus of the detailed analysis presented herein was for SWBLIs at $Re_D = 2 \times 10^6$.

The application of the PIV technique in this test section required meticulous design to provide adequate optical access without disturbing the SWBLI flow. The influence of the non-axisymmetric features required for the application of PIV was quantified and shown to be inconsequential to the results presented. The PIV measurement apparatus is capable of rapidly acquiring data of all 3 velocity components in 2D planes. By translating the camera assembly, data was collected across the entire SWBLI region without interrupting facility operation.

The PIV measurement system in combination with the continuous flow wind tunnel allowed for many snapshots of the velocity field (uncorrelated in time) to be collected for computation of mean and fluctuating components. Comparisons of the mean and r.m.s. velocity in the upstream boundary layer were made with previously obtained probe-based measurements and expected values for a turbulent boundary layer. The challenges in making accurate turbulence particle-based measurements in compressible boundary layers are discussed. PIV datasets from multiple camera positions were collated into panoramic fields of mean and turbulent quantities across the upstream boundary layer, interaction, and recovery region.

In particular, the strength of the stereoscopic PIV measurement applied in this work lies in the ability to resolve three-dimensional velocity vectors. This allows for the determination of the out-of-plane velocity component which is typically very difficult to obtain through probe-based measurement. The PIV data was able to quantify the strong spanwise flow which occurs along the wall in the $\overline{\theta} = 90°$ interaction as well as the associated $\overline{u'w'}$ shear stress. This case provides a unique flowfield in which the three-dimensionality may challenge turbulence models in a new way. Also, because the PIV measurement samples all 3 velocity components simultaneously, the complete kinematic Reynolds stress tensor can be computed. With this data available, the degree and nature of the turbulence anisotropy may be evaluated. In this report, two-dimensional maps of the anisotropy tensor invariants were generated to elucidate how this

behavior varies spatially through the flowfields studied. The axisymmetric case with a weak impinging shock shows very little deviation from the upstream turbulent boundary layer behavior while the separated case showed a distinct deviation toward more isotropic behavior in the recovering boundary layer. In the swept interaction, the near-wall turbulence is distinctly more two-dimensional, implying a lasting influence of the additional x-z shear generated by the strong spanwise flow. The evolution of the turbulence anisotropy provides another benchmark for evaluating the ability of turbulent calculation methods, from Reynolds-averaged Navier-Stokes methods to scale-resolving approaches such as LES, in simulating the detailed behavior of SWBLIs.

An additional asset of the PIV technique is that it supplies continuous planes of data upon which further spatial analyses can be applied. In the present paper, the correlation of turbulence quantities with mean velocity gradient were computed. It was observed that the region of high streamwise turbulence corresponds closely to the region of high $\frac{\partial U}{\partial x}$ in the axisymmetric interaction, which creates a region of strong production of streamwise turbulence. The region of high shear stress was distributed over a larger region and thus less correlated with gradient in the streamwise velocity. In the swept interaction, the same behavior was observed for the streamwise turbulence. However, the primary shear in this interaction occurs in $\overline{u'w'}$ which was found to be the strongest (measured) producer of spanwise turbulence near the separated region. Further downstream in the region of highest spanwise velocity, the character reverses as $\overline{v'w'}\frac{\partial W}{\partial y}$ becomes the dominant shear-based production term. The relative significance of these terms may be compared with the full turbulence budget available in a LES or DNS.

The intent of this work is to provide a publicly available comprehensive dataset in an array of flow configurations which are typically challenging for RANS models. This report points out key flow features that should be targeted when evaluating simulation results. Additionally, some first order analyses were applied to the statistical distributions of turbulent fluctuations to inform where equilibrium models may fail and for comparison with more sophisticated methods, such as hybrid LES/RANS. A repository for this data is in the process of being established to release for public use.

Acknowledgments

Support for this work was provided by NASA's Transformative Aeronautics Concepts Program through the Transformational Tools & Technologies (T^3) Project. Executing the PIV measurements in the 225 cm^2 Wind Tunnel was made possible with by the skilled engineers and technicians of NASA Glenn's Testing Division. John Friscat, John Lucero, Celia Otero, and Brent Seifert's contributions to this work are gratefully acknowledged.

References

[1] DeBonis, J. R., Oberkampf, W. L., Wolf, R. T., Orkwis, P. D., Turner, M. G., Babinsky, H., and Benek, J. A., "Assessment of Computational Fluid Dynamics and Experimental Data for Shock Boundary-Layer Interactions," *AIAA Journal*, Vol. 50, No. 4, 2012, pp. 891–903. doi:10.2514/1.J051341.

[2] Settles, G. S., and Dodson, L. J., "Supersonic and hypersonic shock/boundary-layer interaction database," *AIAA Journal*, Vol. 32, No. 7, 1994, pp. 1377–1383. doi:10.2514/3.12205.

[3] Aeschliman, D. P., and Oberkampf, W. L., "Experimental Methodology for Computational Fluid Dynamics Code Validation," *AIAA Journal*, Vol. 36, No. 5, 1998, pp. 733–741. doi:10.2514/2.461.

[4] Babinsky, H., Oorebeek, J., and Cottingham, T., "Corner effects in reflecting oblique shock-wave/boundary-layer interactions," *51st AIAA Aerospace Sciences Meeting including the New Horizons Forum and Aerospace Exposition*, , No. January, 2013, pp. 1–11. doi:10.2514/6.2013-859.

[5] Garnier, E., "Stimulated detached eddy Simulation of three-dimensional shock/boundary layer interaction," *Shock Waves*, Vol. 19, No. 6, 2009, pp. 479–486. doi:10.1007/s00193-009-0233-7.

[6] Davis, D. O., "CFD Validation Experiment of a Mach 2.5 Axisymmetric Shock-Wave/Boundary-Layer Interaction," *Proceedings of the ASME/JSMA/KSME 2015 Joint Fluids Engineering Conference*, Fluids Engineering Division Summer Meeting, Vol. Volume 1: Symposia, 2015. doi:10.1115/AJKFluids20156342, v001T06A001.

[7] Sasson, J., "Conical Shock Wave Turbulent Boundary Layer Interactions in a Circular Test Section at Mach 2.5," Ph.D. thesis, Case Western Reserve University, 2022. URL http://rave.ohiolink.edu/etdc/view?acc_num=case1648825433614363.

[8] Sasson, J., Reising, H. H., Davis, D. O., and Barnhart, P. J., "Summary of Shock Wave Turbulent Boundary Layer Interaction Experiments In a Circular Test Section," *AIAA SciTech 2023*, 2023. doi:10.2514/6.2023-0442.

[9] Reising, H. H., and Davis, D. O., "Development and Assessment of a New Particle Image Velocimetry System in the NASA GRC 225 cm^2 Wind Tunnel," *AIAA SciTech 2023*, National Harbor, MD, 2023. doi:10.2514/6.2023-0631.

[10] Monkewitz, P. A., Chauhan, K. A., and Nagib, H. M., "Self-consistent high-Reynolds-number asymptotics for zero-pressure-gradient turbulent boundary layers," *Physics of Fluids*, Vol. 19, No. 115101, 2007. doi:10.1063/1.2780196.

[11] Nagib, H. M., Chauhan, K. A., and Monkewitz, P. A., "Approach to an asymptotic state for zero pressure gradient turbulent boundary layers," *Philosophical Transactions of the Royal Society A: Mathematical, Physical and Engineering Sciences*, Vol. 365, No. 1852, 2007, pp. 755–770. doi:10.1098/rsta.2006.1948.

[12] Sun, C.-C., and Childs, M. E., "A modified wall wake velocity profile for turbulent compressible boundary layers." *Journal of Aircraft*, Vol. 10, No. 6, 1973, pp. 381–383. doi:10.2514/3.44376.

[13] Chauhan, K. A., and Nagib, H. M., "On the Composite Logarithmic Profile in Zero Pressure Gradient Turbulent Boundary Layers," *45th AIAA Aerospace Sciences Meeting*, 2007. doi:10.2514/6.2007-532.

[14] Hopkins, E. J., and Inouye, M., "An evaluation of theories for predicting turbulent skin friction andheat transfer on flat plates at supersonic and hypersonic Mach numbers," *AIAA Journal*, Vol. 9, No. 6, 1971, pp. 993–1003. doi:10.2514/3.6323.

[15] Kumar, P., and Mahesh, K., "Analysis of axisymmetric boundary layers," *Journal of Fluid Mechanics*, Vol. 849, 2018, pp. 927–941. doi:10.1017/jfm.2018.449.

[16] Morkovin, M. V., "Effects of compressibility on turbulent flows," *Mécanique de la Turbulence*, Vol. 367, No. 380, 1962, p. 26.

[17] Duan, L., Beekman, I., and Martín, M. P., "Direct numerical simulation of hypersonic turbulent boundary layers. Part 3. Effect of Mach number," *Journal of Fluid Mechanics*, Vol. 672, 2011, pp. 245–267. doi:10.1017/S0022112010005902.

[18] Walz, A., *Boundary layers of flow and temperature*, M.I.T. Press, 1969.

[19] Keane, R. D., and Adrian, R. J., "Optimization of particle image velocimeters. I. Double pulsed systems," *Measurement Science and Technology*, Vol. 1, No. 11, 1990, pp. 1202–1215. doi:10.1088/0957-0233/1/11/013.

[20] Metzger, M. M., and Klewicki, J. C., "A comparative study of near-wall turbulence in high and low Reynolds number boundary layers," *Physics of Fluids*, Vol. 13, No. 3, 2001, pp. 692–701. doi:10.1063/1.1344894.

[21] Marusic, I., and Kunkel, G. J., "Streamwise turbulence intensity formulation for flat-plate boundary layers," *Physics of Fluids*, Vol. 15, No. 8, 2003, pp. 2461–2464. doi:10.1063/1.1589014.

[22] De Graaff, D. B., and Eaton, J. K., "Reynolds-number scaling of the flat-plate turbulent boundary layer," *Journal of Fluid Mechanics*, Vol. 422, 2000, pp. 319–346. doi:10.1017/s0022112000001713.

[23] Marusic, I., McKeon, B. J., Monkewitz, P. A., Nagib, H. M., Smits, A. J., and Sreenivasan, K. R., "Wall-bounded turbulent flows at high Reynolds numbers: Recent advances and key issues," *Physics of Fluids*, Vol. 22, No. 6, 2010, pp. 1–24. doi:10.1063/1.3453711.

[24] Schlatter, P., and Örlü, R., "Assessment of direct numerical simulation data of turbulent boundary layers," *Journal of Fluid Mechanics*, Vol. 659, 2010, pp. 116–126. doi:10.1017/S0022112010003113.

[25] Kunkel, G. J., and Marusic, I., "Study of the near-wall-turbulent region of the high-Reynolds-number boundary layer using an atmospheric flow," *Journal of Fluid Mechanics*, Vol. 548, 2006, pp. 375–402. doi:10.1017/s0022112005007780.

[26] Panton, R. L., "Overview of the self-sustaining mechanisms of wall turbulence," *Progress in Aerospace Sciences*, Vol. 37, No. 4, 2001, pp. 341–383. doi:10.1016/s0376-0421(01)00009-4.

[27] Lowe, K. T., Byun, G., and Simpson, R. L., "The Effect of Particle Lag on Supersonic Turbulent Boundary Layer Statistics," *52nd Aerospace Sciences Meeting*, American Institute of Aeronautics and Astronautics, 2014. doi:10.2514/6.2014-0233.

[28] Williams, O. J., Sahoo, D., Baumgartner, M. L., and Smits, A. J., "Experiments on the structure and scaling of hypersonic turbulent boundary layers," *Journal of Fluid Mechanics*, Vol. 834, 2018, pp. 237–270. doi:10.1017/jfm.2017.712.

[29] Brooks, J. M., Gupta, A. K., Smith, M., Marineau, E., and Tatum, K. E., "High-Speed Local Particle Injection for Particle Image Velocimetry," *AIAA Journal*, Vol. 57, No. 10, 2019, pp. 4490–4503. doi:10.2514/1.J057654.

[30] Aultman, M. T., Disotell, K., and Duan, L., "The Effect of Particle Lag on Statistics of Hypersonic Turbulent Boundary Layers Subject to Pressure Gradients," *AIAA SCITECH 2022 Forum*, American Institute of Aeronautics and Astronautics, 2022. doi:10.2514/6.2022-1062.

[31] Priyadarshana, P. J. A., and Klewicki, J. C., "Study of the motions contributing to the Reynolds stress in high and low Reynolds number turbulent boundary layers," *Physics of Fluids*, Vol. 16, No. 12, 2004, pp. 4586–4600. doi:10.1063/1.1809131.

[32] Williams, O. J., Nguyen, T., Schreyer, A.-M., and Smits, A. J., "Particle response analysis for particle image velocimetry in supersonic flows," *Physics of Fluids*, Vol. 27, No. 7, 2015, p. 076101. doi:10.1063/1.4922865.

[33] Loth, E., "Compressibility and Rarefaction Effects on Drag of a Spherical Particle," *AIAA Journal*, Vol. 46, No. 9, 2008, pp. 2219–2228. doi:10.2514/1.28943.

[34] Davies, C. N., "Definitive equations for the fluid resistance of spheres," *Proceedings of the Physical Society*, Vol. 57, No. 4, 1945, pp. 259–270. doi:10.1088/0959-5309/57/4/301.

[35] Mosele, J.-P., Gross, A., and Slater, J., "Numerical Investigation of Asymmetric Mach 2.5 Turbulent Shock Wave Boundary Layer Interaction," *Aerospace*, Vol. 10, No. 5, 2023, p. 417. doi:10.3390/aerospace10050417.

[36] Humble, R. A., Scarano, F., and Van Oudheusden, B. W., "Particle image velocimetry measurements of a shock wave/turbulent boundary layer interaction," *Experiments in Fluids*, Vol. 43, No. 2-3, 2007, pp. 173–183. doi:10.1007/s00348-007-0337-8.

[37] Lumley, J. L., and Newman, G. R., "The return to isotropy of homogeneous turbulence," *Journal of Fluid Mechanics*, Vol. 82, No. 1, 1977, pp. 161–178. doi:10.1017/s0022112077000585.

[38] Choi, K.-S., and Lumley, J. L., "The return to isotropy of homogeneous turbulence," *Journal of Fluid Mechanics*, Vol. 436, 2001, pp. 59–84. doi:10.1017/s002211200100386x.

[39] Banerjee, S., Krahl, R., Durst, F., and Zenger, C., "Presentation of anisotropy properties of turbulence, invariants versus eigenvalue approaches," *Journal of Turbulence*, Vol. 8, 2007, p. N32. doi:10.1080/14685240701506896.

[40] Emory, M., and Iaccarino, G., "Visualizing turbulence anisotropy in the spatialdomain with componentality contours," Tech. rep., Stanford Center for Turbulence Research Annual Resarch Briefs, 2014.

[41] Morgan, B., Duraisamy, K., Nguyen, N., Kawai, S., and Lele, S. K., "Flow physics and RANS modelling of oblique shock/turbulent boundary layer interaction," *Journal of Fluid Mechanics*, Vol. 729, 2013, pp. 231–284. doi:10.1017/jfm.2013.301.

[42] Chou, J., Childs, M., and Wong, R., "An experimental study of three-dimensional shock wave/turbulent boundary layer interactions in a supersonic flow," *18th Fluid Dynamics and Plasmadynamics and Lasers Conference*, American Institute of Aeronautics and Astronautics, 1985. doi:10.2514/6.1985-1566.

[43] Wieneke, B., "PIV uncertainty quantification from correlation statistics," *Measurement Science and Technology*, Vol. 26, No. 7, 2015. doi:10.1088/0957-0233/26/7/074002.

[44] Scharnowski, S., Bross, M., and Kähler, C. J., "Accurate turbulence level estimations using PIV/PTV," *Experiments in Fluids*, Vol. 60, 2019, pp. 1–12. doi:10.1007/s00348-018-2646-5.

[45] Wieneke, B., "Stereo-PIV using self-calibration on particle images," *Experiments in Fluids*, Vol. 39, 2005, pp. 267–280. doi:10.1007/s00348-005-0962-z.